Finite Elements in Analysis and Design 192 (2021) 103538

Contents lists available at ScienceDirect

Finite Elements in Analysis and Design

journal homepage: www.elsevier.com/locate/finel

A simple and computationally efficient stress integration scheme based on numerical approximation of the yield function gradients: Application to advanced yield criteria

N. Hosseini, J.A. Rodríguez-Martínez *

Department of Continuum Mechanics and Structural Analysis, University Carlos III of Madrid, Avda. de la Universidad, 30, 28911, Leganés, Madrid, Spain

ARTICLE INFO

Keywords:
Advanced yield criteria
Anisotropy
Stress integration
Finite elements
Metal forming

ABSTRACT

In this paper, we have modified the stress integration scheme proposed by Choi and Yoon [1]; which is based on the numerical approximation of the yield function gradients, to implement in the finite element code ABAQUS three elastic isotropic, plastic anisotropic constitutive models with yielding described by Yld2004-18p [2], CPB06ex2 [3] and Yld2011-27p [4] criteria, respectively. We have developed both VUMAT and UMAT subroutines for the three constitutive models, and have carried out cylindrical cup deep drawing test simulations and calculations of dynamic necking localization under plane strain tension, using explicit and implicit analyses. An original feature of this paper is that these finite element simulations are systematically compared with additional calculations performed using (i) the numerical approximation scheme developed by Choi and Yoon [1]; and (ii) the analytical computation of the first and second order yield functions gradients. This comparison has shown that the numerical approximation of the yield function gradients proposed in this paper facilitates the implementation of the constitutive models, and in the case of the implicit analyses, it leads to a significant decrease of the computational time without impairing the accuracy of the finite element results. In addition, we have demonstrated that there is a critical loading rate below which the dynamic implicit analyses are computationally more efficient than the explicit calculations.

1. Introduction

The pioneering work of Hill [5] was a turning point in the mathematical theory of anisotropic plasticity. By analogy with the von Mises[6] yield criterion for isotropic materials, Hill [5] proposed a quadratic yield function to model the macroscopic behaviour of orthotropic metals which depends only on the deviatoric stresses and is pressure independent. The model highlights due to its simplicity, versatility and easy calibration procedure; so that 70 years after its publication, the criterion of Hill [5] still is the anisotropic model most widely used to describe the directionality of plastic properties of metallic materials used in scientific and technological applications [7–12]. However, due to the fact that Hill's yield function is quadratic in stresses and contains *only* six independent parameters to describe the state of anisotropy, it cannot capture with the same accuracy both the yield stress and Lankford coefficients [13,14]. Hill [15] acknowledged what he referred to as *inevitable limitations in the range of validity of the 1948 prototype* and proposed an improved yield criterion based on arbitrary linear combinations of equal non-integer powers of the principal values of the deviatoric stress, together with the same powers of their differences. This criterion, specifically developed to describe the mechanical response of textured sheets for situations in which the orthotropy and the loading are co-directional [16,17], included 7 parameters to describe material anisotropy, and provided extended flexibility without sacrificing too much of the simplicity that was a main attraction of the 1948 proposal. Nevertheless, nor the original model, neither the 1979 improvement can describe the mechanical response of materials which exhibit complex plastic anisotropy.

Many yield functions have been developed over the years to improve the formulations of Hill [5,15]. For instance, Barlat and Lian [18] extended to orthotropy the 2D model of Barlat and Lian [19] using a linear transformation of the components of the stress tensor. The anisotropic criterion of Barlat and Lian [18] captured the behavior of orthotropic sheet metals under a full plane stress state including 4 independent material parameters, and showed remarkable capacity to describe the yield surfaces computed with the Bishop and Hill

* Corresponding author.
E-mail address: jarmarti@ing.uc3m.es (J.A. Rodríguez-Martínez).

https://doi.org/10.1016/j.finel.2021.103538
Received 3 August 2020; Received in revised form 12 November 2020; Accepted 18 January 2021
Available online 1 March 2021

[20] polycrystal model. Shortly after, Barlat et al. [21] extended to orthotropic anisotropy the isotropic criterion proposed by Hosford [22] in order to generalize the 2D model of Barlat and Lian [18] to any complex three-dimensional stress state. However, the criterion of Barlat et al.[21] cannot be used for materials with symmetries other than the orthotropic symmetry. This motivated to Karafillis and Boyce [23] to propose a non-quadratic yield criterion capable of describing different states of material symmetry, including the most generalized case of the totally asymmetric material. Following previous ideas of Barlat and Lian [18] and Barlat et al. [21]; among others, Karafillis and Boyce [23] used a fourth order tensor as a linear multiplicative operator acting on the stress tensor to introduce material anisotropy. The predictions of the model of Karafillis and Boyce [23] were found to be in good agreement with experimental results for a variety of materials. The fourth order tensorial operator introduced by Karafillis and Boyce [23] was further used by Barlat et al. [24] to improve the model developed in Barlat et al. [21]; introducing three additional material parameters which provided increased flexibility to describe the anisotropic response of different materials. The model of Barlat et al. [24] was demonstrated to be particularly valid for materials which exhibit large pure shear yield stress.

Following the works of Karafillis and Boyce [23] and Barlat et al. [24]; the linear transformation-based anisotropic yield functions became increasingly popular because, among other reasons, they allow *tailoring* the number of anisotropy parameters without significant impact on the mathematical structure of the constitutive model. Barlat et al. [25] developed a plane stress yield function with 9 parameters to describe the mechanical response of aluminum sheets using two linear transformations of the Cauchy stress tensor. It was shown that the accuracy in the description of the flow stress anisotropy and Lankford coefficients is increased as the number of linear transformations, and thus the number of anisotropy parameters, increases. Bron and Besson [26] extended the models of Barlat et al. [21] and Karafillis and Boyce [23] using two linear transformations. The resulting 3D yield function, that was demonstrated to be convex, contained 16 parameters and provided accurate description of the plastic anisotropy of various aluminum sheet samples. Two linear transformations were also used by Barlat et al. [2] to formulate the so-called Yld2004-13p and Yld2004-18p yield functions. These two anisotropic models were derived from different isotropic criteria, so that they contain 13 and 18 anisotropic parameters, respectively. The values of these parameters were computed for 2090-T3 and 6111-T4 aluminum alloys. The comparison between yield functions predictions and experiments showed that both models capture the main features of the anisotropic behaviour of 2090-T3 and 6111-T4. Notably, the Yld2004-18p model described very accurately the flow stresses in uniaxial tension and the Lankford coefficients of both sheet materials. Two and three linear transformations were used by Aretz and Barlat [4] to obtain the so-called Yld2011-18p and Yld2011-27p yield functions, which contain 18 and 27 parameters, respectively. While the Yld2011-18p model can be regarded as complementary to the yield function Yld2004-18p proposed few years earlier (same number of parameters but different behavior during calibration of the experimental data), the Yld2011-27p provided extended flexibility and improved accuracy to describe the complex plastic anisotropy of AA 2090-T3 and AA 3104-H19.

Most of the anisotropic yield criteria cited so far were specifically developed to model metals with cubic structure. Hence, they are usually represented by even functions of stresses and do not capture the tension/compression asymmetry in yielding characteristic of hexagonal closed packed metals. Cazacu and Barlat [27] proposed a yield criterion to describe both the asymmetry and anisotropy in yielding of magnesium and magnesium alloys using the generalized invariants approach developed by Cazacu and Barlat [28]. The yield function of Cazacu and Barlat [27] is an homogeneous function of degree three in stresses and contains 18 material parameters. Shortly after, Cazacu et al. [29] developed the so-called CPB06 yield criterion, in which the degree of homogeneity is a material parameter to be determined, to capture simultaneously the anisotropy and tension/compression asymmetry of hexagonal closed packed metals. Similarly to Karafillis and Boyce [23] and Barlat et al. [24]; the anisotropy was introduced using a linear transformation of the stress deviator. For 3D stress conditions, this yield criterion involves 9 independent anisotropy coefficients, 1 parameter to describe the strength differential effect and 1 more to determine the degree of homogeneity of the yield function. Plunkett et al. [3] extended the CPB06 model using two linear transformations and derived the so-called CPB06ex2 yield criterion which contains a total of 21 parameters, and represents with great accuracy both the tensile and compressive anisotropy in yield stresses and Lankford coefficients of materials with hcp crystal structure and of metal sheets with cubic crystal structure. During the last few years, additional yield functions to model the anisotropy and tension/compression asymmetry in yielding of various metallic materials have been proposed, for instance, by Nixon et al. [30]; Khan et al. [31]; Raemy et al. [32]; Kondori et al. [33]; Park et al. [34]; Sanz et al. [35] and Lee et al. [36].

As a general rule, the ability of the yield functions to describe complex anisotropic and tension/compression asymmetric behaviors increases with the number of material parameters. However, accuracy comes with a price. As the number of parameters increases: (i) larger number of tests is needed to determine the material parameters (if experimental data are not available, modelers also rely on numerical data obtained from polycrystalline calculations, see Yoon et al. [37] and Grytten et al. [38]), (ii) the implementation of the yield functions in finite element codes becomes an increasingly laborious task and (iii) the computational efficiency decreases. In particular, a key step in the finite element implementation process is the computation of the yield function gradients (i.e. the derivatives of the effective stress with respect to the stress components) which are required to calculate the effective plastic strain increment and the tangent stiffness tensor, the latter being necessary in implicit finite element solutions (e.g. Yoon et al. [39] and Vadillo et al. [40]). For advanced yield criteria, in which anisotropy is included using more than one linear transformation (see previous paragraphs of this introductory section), the analytical forms of the first and second order yield function gradients are lengthy and complex expressions, which increases the difficulties associated to the implementation of constitutive models in finite element codes. In order to alleviate this problem, Aretz [41] proposed to use numerical approximations of the yield function gradients, which is also an effective way to get rid of the singularities that appear in their analytical counterparts [2,4]. Very recently, Choi and Yoon [1] modified the stress integration algorithm developed by Aretz [41] to implement in ABAQUS/Standard various anisotropic constitutive models with distortional hardening under associated and non-associated flow rules. In addition, the simple mathematical form of the numerical approximations suggests that their application in the finite element implementation process could lead to significant computational time reduction, facilitating the utilization of advanced yield functions in large scale numerical simulations. Nevertheless, to the authors' knowledge, the *anticipated* computational efficiency of using numerical approximations of the yield function gradients has not been thoroughly investigated so far. In this regard, note that Choi and Yoon [1] only performed relatively small simulations: single element calculations to evaluate the accuracy of the numerical approximations of the yield function gradients, and deep drawing calculations where the blank is modeled with a maximum of 2000 elements to check the number of ears predicted by the various constitutive models investigated.

In this paper, we modify the numerical differentiation schemes proposed by Aretz [41] and Choi and Yoon [1] to implement in the finite element code ABAQUS three elastic isotropic, plastic anisotropic constitutive models with yielding described by Yld2004-18p, CPB06ex2 and Yld2011-27p criteria, respectively. We have developed VUMAT and UMAT subroutines for the three constitutive models, using both the analytical expressions and the numerical approximations of the first and second order yield function gradients. We have carried out cylindri-

cal cup deep drawing test simulations using the configuration reported in Yoon et al. [37]; and calculations of dynamic necking localization under plane strain tension with the finite element model developed by N'souglo et al. [42]; using both implicit and explicit analyses. We have identified that there is a critical loading rate below which the dynamic implicit analyses are computationally more efficient than the explicit calculations. Moreover, the systematic comparison between the finite element results obtained with the analytical expressions and the numerical approximations of the yield functions gradients has shown that, while in the case of the explicit analyses using a VUMAT the procedure used to calculate the stress derivatives hardly affects the computational time, the utilization of the numerical approximations in implicit analyses using a UMAT indeed leads to an important decrease of the computational cost. This decrease reaches up to 70% for some of the numerical simulations presented in this paper, and it increases as the number of elements in the finite element mesh increases. We have also shown that the computational time required for the dynamic necking calculations is between 5% and 45% smaller for the numerical differentiation scheme proposed in this work in comparison with the formulation developed by Choi and Yoon [1].

2. Constitutive framework

We consider three elastic isotropic, plastic orthotropic constitutive models with yielding described by Yld2004-18p [2], CPB06ex2 [3] and Yld2011-27p [4] criteria, respectively. These advanced yield criteria were specifically developed to capture the mechanical response of highly textured metallic materials which exhibit complex plastic anisotropy. Section 2.1 sets out the general formulation of the three constitutive models, while the specific features of each yield criterion are shown in Sections 2.2, 2.3 and 2.4, respectively.

2.1. Basic features of the constitutive models

Elasto-plastic constitutive equations in finite element codes for large deformation solid mechanical applications are mostly based on an *ad hoc* extension of classical small-strain elasto-plasticity to the finite deformation range. We assume the additive decomposition of the total rate of deformation tensor $\mathbf{d}$ into an elastic part $\mathbf{d}_e$ and a plastic part $\mathbf{d}_p$:

$$\mathbf{d} = \mathbf{d}_e + \mathbf{d}_p \tag{1}$$

where the elastic part of the rate of deformation tensor is related to the rate of the stress by the following linear elastic law:

$$\overset{\triangledown}{\boldsymbol{\sigma}} = \mathbf{L} : \mathbf{d}_e \tag{2}$$

where $\overset{\triangledown}{\boldsymbol{\sigma}}$ is an objective derivative of the Cauchy stress tensor, and $\mathbf{L}$ is the tensor of isotropic elastic moduli given by:

$$\mathbf{L} = 2G\mathbf{I}' + K\mathbf{1}\otimes\mathbf{1} \tag{3}$$

with $\mathbf{1}$ and $\mathbf{I}'$ being the unit second-order tensor and the unit deviatoric fourth-order tensor, respectively. Moreover G and K are the shear modulus and the bulk modulus (they are assumed constant).

In order to achieve incremental objectivity of the constitutive equations, ABAQUS considers the objective stress derivative to be defined as:

$$\overset{\triangledown}{\boldsymbol{\sigma}} = \dot{\boldsymbol{\sigma}} + \boldsymbol{\sigma}\boldsymbol{\omega} - \boldsymbol{\omega}\boldsymbol{\sigma} \tag{4}$$

where $\boldsymbol{\omega}$ is a skew-symmetric tensor so that $\overset{\triangledown}{\boldsymbol{\sigma}}$ coincides with the Green-Naghdi objective derivative used by ABAQUS/Explicit if $\boldsymbol{\omega} = \boldsymbol{\Omega}$, where $\boldsymbol{\Omega} = \dot{\mathbf{R}}\mathbf{R}^T$ with $\mathbf{R}$ being the polar rotation tensor, and with the Jaumann objective derivative used by ABAQUS/Standard if $\boldsymbol{\omega} = \boldsymbol{w}$, where $\boldsymbol{w}$ is the spin tensor (i.e. the skew-symmetric part of the velocity gradient tensor). Note that $\dot{(\,)}$ denotes differentiation with respect to time.

The general expression for the yield criteria considered in this paper is:

$$\phi = \phi\left(\widetilde{S}'_i, \widetilde{S}''_i, \widetilde{S}'''_i\right) \tag{5}$$

where $\left(\widetilde{S}'_i, \widetilde{S}''_i, \widetilde{S}'''_i\right)$, with $i = 1,2,3$ (see equation (8)), are the principal values of the second order deviatoric tensors $\widetilde{\mathbf{s}}'$, $\widetilde{\mathbf{s}}''$ and $\widetilde{\mathbf{s}}'''$, which are defined by three linear transformations:

$$\widetilde{\mathbf{s}}' = \mathbf{C}'\mathbf{s} \tag{6a}$$

$$\widetilde{\mathbf{s}}'' = \mathbf{C}''\mathbf{s} \tag{6b}$$

$$\widetilde{\mathbf{s}}''' = \mathbf{C}'''\mathbf{s} \tag{6c}$$

where $\mathbf{s}$ is the deviatoric part of the Cauchy stress tensor $\boldsymbol{\sigma}$, and $\mathbf{C}'$, $\mathbf{C}''$ and $\mathbf{C}'''$ are the matrices which contain the anisotropy coefficients:

$$\mathbf{C}' = \begin{bmatrix} -c'_{11} & -c'_{12} & -c'_{13} & 0 & 0 & 0 \\ -c'_{21} & -c'_{22} & -c'_{23} & 0 & 0 & 0 \\ -c'_{31} & -c'_{32} & -c'_{33} & 0 & 0 & 0 \\ 0 & 0 & 0 & c'_{44} & 0 & 0 \\ 0 & 0 & 0 & 0 & c'_{55} & 0 \\ 0 & 0 & 0 & 0 & 0 & c'_{66} \end{bmatrix} \tag{7a}$$

$$\mathbf{C}'' = \begin{bmatrix} -c''_{11} & -c''_{12} & -c''_{13} & 0 & 0 & 0 \\ -c''_{21} & -c''_{22} & -c''_{23} & 0 & 0 & \\ -c''_{31} & -c''_{32} & -c''_{33} & 0 & 0 & 0 \\ 0 & 0 & 0 & c''_{44} & 0 & 0 \\ 0 & 0 & 0 & 0 & c''_{55} & 0 \\ 0 & 0 & 0 & 0 & 0 & c''_{66} \end{bmatrix} \tag{7b}$$

$$\mathbf{C}''' = \begin{bmatrix} -c'''_{11} & -c'''_{12} & -c'''_{13} & 0 & 0 & 0 \\ -c'''_{21} & -c'''_{22} & -c'''_{23} & 0 & 0 & 0 \\ -c'''_{31} & -c'''_{32} & -c'''_{33} & 0 & 0 & 0 \\ 0 & 0 & 0 & c'''_{44} & 0 & 0 \\ 0 & 0 & 0 & 0 & c'''_{55} & 0 \\ 0 & 0 & 0 & 0 & 0 & c'''_{66} \end{bmatrix} \tag{7c}$$

with c'_{ij}, c''_{ij} and c'''_{ij} being material parameters. Note that for Yld2004-18p and Yld2011-27p yield criteria $c'_{ii} = c''_{ii} = c'''_{ii} = 0$ with $i = 1,2,3$ (see Sections 2.2 and 2.4), i.e. for these two constitutive models the matrices which contain the anisotropy coefficients only have 9 non-zero coefficients. In equation (6), we have taken the order of the components of the column vector representing the deviatoric stress tensor to be $\mathbf{s} = \{s_{11}\ s_{22}\ s_{33}\ s_{23}\ s_{31}\ s_{12}\}$, with the Cartesian coordinate system $(1,2,3)$ being associated to the orthotropy axes of the material (1, 2 and 3 axes correspond to the rolling, transverse and normal directions, respectively).

The ordered principal values of the tensor $\widetilde{\mathbf{s}}'$ are:

$$\widetilde{S}'_1 = 2\sqrt{\left(H'_1\right)^2 + H'_2}\cos\left(\frac{\theta}{3}\right) + H'_1 \tag{8a}$$

$$\widetilde{S}'_2 = 2\sqrt{\left(H'_1\right)^2 + H'_2}\cos\left(\frac{\theta+4\pi}{3}\right) + H'_1 \tag{8b}$$

$$\widetilde{S}'_3 = 2\sqrt{\left(H'_1\right)^2 + H'_2}\cos\left(\frac{\theta+2\pi}{3}\right) + H'_1 \tag{8c}$$

with $\theta = \arccos\left(\frac{q}{p^{\frac{3}{2}}}\right)$, $p = \left(H_1'\right)^2 + H_2'$ and $q = \frac{2\left(H_1'\right)^3 + 3H_1'H_2' + 2H_3'}{2}$, where H_1', H_2' and H_3' are the 1st, 2nd and 3rd invariants of $\widetilde{\mathbf{s}}'$. Analogous procedure is followed to obtain the principal values of the tensors $\widetilde{\mathbf{s}}''$ and $\widetilde{\mathbf{s}}'''$.

Moreover, the yield condition is expressed as:

$$f = \bar{\sigma} - \sigma_Y = 0 \tag{9}$$

where $\bar{\sigma} = \bar{\sigma}(\phi)$ is the effective stress (the specific form of $\bar{\sigma}$ for the three yield criteria considered is given in equations (19), (21) and (25)) and σ_Y is the tensile yield stress in the rolling direction (see also equations (19), (21) and (25)). The hardening of the material, which is considered to be isotropic and governed by the effective plastic strain $\bar{\varepsilon}_p$, is assumed to be of the form:

$$\sigma_Y = \sigma^0\left(\varepsilon^0 + \bar{\varepsilon}_p\right)^n \tag{10}$$

where σ^0, ε^0, and n are material parameters, see Table 1.

The effective plastic strain is defined as:

$$\bar{\varepsilon}_p = \int_0^t \dot{\bar{\varepsilon}}_p d\tau \tag{11}$$

with $\dot{\bar{\varepsilon}}_p$ being the work-conjugate of the specific effective stress associated to the yield criterion (see equations (19), (21) and (25)). Recall that a superposed dot denotes differentiation with respect to time.

Moreover, assuming an associated plastic flow rule, the plastic part of the rate of deformation tensor is:

$$\boldsymbol{d}_p = \dot{\lambda}\frac{\partial \bar{\sigma}}{\partial \boldsymbol{\sigma}} \tag{12}$$

where $\dot{\lambda}$ is the rate of plastic multiplier.

Since the effective stress is a first order homogeneous function in stress (see equations (19), (21) and (25)), we have from the Euler's homogeneous function theorem that:

$$\bar{\sigma} = \boldsymbol{\sigma} : \frac{\partial \bar{\sigma}}{\partial \boldsymbol{\sigma}} \tag{13}$$

Therefore, the work conjugacy relation:

$$\boldsymbol{\sigma} : \boldsymbol{d}_p = \bar{\sigma}\dot{\bar{\varepsilon}}_p \tag{14}$$

leads to the identity:

$$\dot{\bar{\varepsilon}}_p = \dot{\lambda} \tag{15}$$

The formulation of the constitutive model is completed with the Kuhn-Tucker loading-unloading conditions:

$$\dot{\lambda} \geqslant 0, \qquad f \leqslant 0, \qquad \dot{\lambda} f = 0 \tag{16}$$

and the consistency condition during plastic loading:

$$\dot{f} = 0 \tag{17}$$

Table 1 shows the initial density, the elastic constants, and the hardening parameters used in the finite element simulations shown in Section 7. The parameters values correspond to AA 2090-T3 and they are taken from Yoon et al. [37] and Cvitanić et al. [43].

Table 1
Initial density, elastic constants and strain hardening parameters for AA 2090-T3. Data after Yoon et al. [3,7] and Cvitanić et al. [43].

Symbol	Property and units	Value
ρ^0	Initial density (kg/m^3)	2700
G	Elastic shear modulus (GPa), Eq. (4)	26.92
K	Bulk modulus (GPa), Eq. (4)	58.33
σ^0	Material parameter (MPa), Eq. (10)	646
ε^0	Material parameter, Eq. (10)	0.025
n	Material parameter, Eq. (10)	0.227

2.2. Yld2004-18p yield criterion

The anisotropy is introduced using 2 linear transformations of the stress deviator, equations (6a) and (6b), which provide 18 anisotropy coefficients, equations (7a) and (7b), whose values must be determined from experiments (recall that for Yld2004-18p yield criterion $c'_{ii} = c''_{ii} = 0$, with $i = 1, 2, 3$, and therefore the matrices $\mathbf{C}'$ and $\mathbf{C}''$ *only* have 9 non-zero coefficients). Note that, if $\mathbf{C}' = \mathbf{C}''$, i.e. if the formulation accounts for only one linear transformation, the Yld2004-18p criterion reduces to the Yld91 model [21], provided that $c'_{12} = c'_{21}$, $c'_{13} = c'_{31}$ and $c'_{32} = c'_{23}$.

The yield function is:

$$\phi_{\text{Yld04}} = \sum_{i=1}^{3}\sum_{j=1}^{3}\left|\widetilde{S}'_i - \widetilde{S}''_i\right|^a \tag{18}$$

and the associated effective stress is:

$$\bar{\sigma} = \left(\frac{\phi_{\text{Yld04}}}{\xi}\right)^{\frac{1}{a}} \tag{19}$$

with $\xi = 4$, so that $\bar{\sigma}$ reduces to the yield stress in the rolling direction (see equation (9)).

The parameters values corresponding to AA 2090-T3 are given in Table 2.

2.3. CPB06ex2 yield criterion

The model accounts for both the anisotropy and tension-compression asymmetry of the material, which are introduced, as in the case of the Yld2004-18p model [2], using 2 linear transformations of the stress deviator (equation (6a) and (6b)). The CPB06ex2 yield criterion contains 21 parameters: 18 to describe the anisotropy (c'_{ij} and c''_{ij} in equations (7a) and (7b)), 2 for the tension-compression asymmetry (k' and k'' in equation (20)), and 1 to determine the degree of homogeneity of the yield function. Note that when $\mathbf{C}' = \mathbf{C}''$ and $k' = k''$, the CPB06ex2 model reduces to the yield criterion developed by Cazacu et al. [29].

The yield function is:

$$\phi_{\text{CPB06}} = \sum_{i=1}^{3}(|\widetilde{S}'_i| - k'\widetilde{S}'_i)^a + \sum_{i=1}^{3}(|\widetilde{S}''_i| - k''\widetilde{S}''_i)^a \tag{20}$$

and the associated effective stress is:

$$\bar{\sigma} = \left(\frac{\phi_{\text{CPB06}}}{\eta}\right)^{\frac{1}{a}} \tag{21}$$

with

$$\eta = \sum_{i=1}^{3}(|\varphi'_i| - k'\varphi'_i)^a + \sum_{i=1}^{3}(|\varphi''_i| - k''\varphi''_i)^a \tag{22}$$

where

$$\begin{aligned}
\varphi'_1 &= \frac{-(2c'_{11} - c'_{12} - c'_{13})}{3}, & \varphi'_2 &= \frac{-(2c'_{12} - c'_{22} - c'_{23})}{3}, \\
& & \varphi'_3 &= \frac{-(2c'_{13} - c'_{23} - c'_{33})}{3} \\
\varphi''_1 &= \frac{-(2c''_{11} - c''_{12} - c''_{13})}{3}, & \varphi''_2 &= \frac{-(2c''_{12} - c''_{22} - c''_{23})}{3}, \\
& & \varphi''_3 &= \frac{-(2c''_{13} - c''_{23} - c''_{33})}{3}
\end{aligned} \tag{23}$$

Notice that the function η is such that $\bar{\sigma}$ reduces to the tensile yield stress in the rolling direction (see equation (9)).

The parameters values corresponding to AA 2090-T3 are given in Table 3.

Table 2
YLD2004-18p yield criterion. Parameters values for AA 2090-T3. Data after Barlat et al. [2].

Anisotropy parameters											
c'_{11}	c'_{12}	c'_{13}	c'_{21}	c'_{22}	c'_{23}	c'_{31}	c'_{32}	c'_{33}	c'_{44}	c'_{55}	c'_{66}
0	−0.06989	0.93640	0.07914	0	1.00306	0.524741	1.36318	0	1.02377	1.06906	0.95432
c''_{11}	c''_{12}	c''_{13}	c''_{21}	c''_{22}	c''_{23}	c''_{31}	c''_{32}	c''_{33}	c''_{44}	c''_{55}	c''_{66}
0	0.98117	0.47674	0.57531	0	0.86682	1.14501	−0.07929	0	1.05166	1.14700	1.40462
Degree of homogeneity of the yield function											
a											
8											

Table 3
CPB06ex2 yield criterion. Parameters values for AA 2090-T3. Data after Plunkett et al.[3].

Anisotropy parameters					
c'_{11}	$c'_{12} = c'_{21}$	$c'_{13} = c'_{31}$	c'_{22}	$c'_{23} = c'_{32}$	c'_{33}
0.453	0.841	1.248	1.058	2.284	3.201
c'_{44}	c'_{55}	c'_{66}	c''_{11}	$c''_{12} = c''_{21}$	$c''_{13} = c''_{31}$
−1	−1	−1.026	−0.453	0.705	−1.148
c''_{22}	$c''_{23} = c''_{32}$	c''_{33}	c''_{44}	c''_{55}	c''_{66}
−0.139	0.519	−0.878	−1	−1	−1.978
Degree of homogeneity of the yield function					
a					
12					
Tension-compression asymmetry parameters					
k'	k''				
0.054	0.027				

2.4. Yld2011-27p yield criterion

The anisotropy is introduced using 3 linear transformations of the stress deviator, equations (6a)-(6c), leading to 27 anisotropy coefficients, equations (7a)-(7c), thereby providing extended flexibility to capture the mechanical response of materials with complex anisotropic behaviour. Recall that for the Yld2011-27p model $c'_{ii} = c''_{ii} = c'''_{ii} = 0$, with $i = 1, 2, 3$.

The yield function is:

$$\phi_{\text{Yld11}} = \sum_{i=1}^{3}\sum_{j=1}^{3}\left|\widetilde{S}'_i + \widetilde{S}''_i\right|^a + \sum_{k=1}^{3}\left|\widetilde{S}'''_i\right|^a \tag{24}$$

and the associated effective stress is:

$$\bar{\sigma} = \left(\frac{\phi_{\text{Yld11}}}{\zeta}\right)^{\frac{1}{a}} \tag{25}$$

with

$$\zeta = \left(\frac{4}{3}\right)^a + 5\left(\frac{2}{3}\right)^a + 6\left(\frac{1}{3}\right)^a \tag{26}$$

Similarly to the Yld2004-18p and CPB06ex2 criteria, the function ζ is chosen so that $\bar{\sigma}$ reduces to the yield stress in the rolling direction (see equation (9)).

The parameters values corresponding to AA 2090-T3 are given in Table 4.

3. Integration of the constitutive equations

The numerical integration is a strain-driven process where the increment of the total strain tensor $\triangle\boldsymbol{\epsilon}$ is given at a quadrature point, and the stress tensor should be updated for the corresponding time increment. The incremental integration is local in space and occurs at each quadrature point inside the finite elements. The three constitutive models presented in Section 2 have been implemented in ABAQUS/Explicit and ABAQUS/Standard through user subroutines VUMAT and UMAT, respectively, using the classical return mapping scheme [44,45]. The specific algorithms used in the VUMAT and UMAT subroutines are shown in Sections 3.1 and 3.2, respectively. The goal is to calculate the increment of the effective plastic strain which is required to update the stress state. In what follows, superscripts n and $n+1$ denote the previous and current time steps, respectively. The return is performed at time $n+1$.

3.1. Convex cutting-plane algorithm

We rewrite the yield condition as:

$$f^{n+1} = \bar{\sigma}^{n+1} - \sigma_Y^{n+1} = 0 \tag{27}$$

The preceding relation is a non-linear algebraic equation in $\triangle\bar{\varepsilon}_p$ which can be solved using an iterative Newton-Raphson procedure. For that purpose, the previous expression is linearized as follows:

$$f^{n+1}_{(k+1)} \approx f^{n+1}_{(k)} + \left(\frac{\partial f}{\partial\bar{\sigma}^{n+1}}\frac{\partial\bar{\sigma}^{n+1}}{\partial\boldsymbol{\sigma}^{n+1}}\frac{\partial\boldsymbol{\sigma}^{n+1}}{\partial\triangle\bar{\varepsilon}_p}\right)_{(k)}\delta\bar{\varepsilon}_{p(k)}$$
$$+\left(\frac{\partial f}{\partial\sigma_Y^{n+1}}\frac{\partial\sigma_Y^{n+1}}{\partial\bar{\varepsilon}_p^{n+1}}\frac{\partial\bar{\varepsilon}_p^{n+1}}{\partial\triangle\bar{\varepsilon}_p}\right)_{(k)}\delta\bar{\varepsilon}_{p(k)} = 0 \tag{28}$$

where k stands for the iterative index and:

$$\frac{\partial f}{\partial\bar{\sigma}^{n+1}} = 1, \qquad \frac{\partial\boldsymbol{\sigma}^{n+1}}{\partial\triangle\bar{\varepsilon}_p} = -\mathbf{L} : \frac{\partial\bar{\sigma}^{n+1}}{\partial\boldsymbol{\sigma}^{n+1}}$$
$$\frac{\partial f}{\partial\sigma_Y^{n+1}} = -1, \qquad \frac{\partial\bar{\varepsilon}_p^{n+1}}{\partial\triangle\bar{\varepsilon}_p} = 1 \tag{29}$$

From equation (28), $\delta\bar{\varepsilon}_{p(k)}$ is calculated as:

$$\delta\bar{\varepsilon}_{p(k)} = \left.\frac{f}{\frac{\partial\bar{\sigma}}{\partial\boldsymbol{\sigma}} : \mathbf{L} : \frac{\partial\bar{\sigma}}{\partial\boldsymbol{\sigma}} + \frac{\partial\sigma_Y}{\partial\bar{\varepsilon}_p}}\right|_{\bullet^{n+1}_{(k)}} \tag{30}$$

where $\bullet^{n+1}_{(k)}$ denotes that $\delta\bar{\varepsilon}_{p(k)}$ is computed at the current time step $n+1$ for a given iteration k.

Table 4
Yld2011-27p yield criterion. Parameters values for AA 2090-T3. Data after Aretz and Barlat [4].

Anisotropy parameters											
c'_{11}	c'_{12}	c'_{13}	c'_{21}	c'_{22}	c'_{23}	c'_{31}	c'_{32}	c'_{33}	c'_{44}	c'_{55}	c'_{66}
0	0.12667	1.29525	0.28407	0	1.42858	0.604524	1.36079	0	1	1	0.8364
c''_{11}	c''_{12}	c''_{13}	c''_{21}	c''_{22}	c''_{23}	c''_{31}	c''_{32}	c''_{33}	c''_{44}	c''_{55}	c''_{66}
0	1.44953	0.99770	1.34779	0	1.00332	1.78676	−0.08678	0	1	1	1
c'''_{11}	c'''_{12}	c'''_{13}	c'''_{21}	c'''_{22}	c'''_{23}	c'''_{31}	c'''_{32}	c'''_{33}	c'''_{44}	c'''_{55}	c'''_{66}
0	−0.61319	0.39240	−1.31670	0	−2.31010	0.72917	0.75833	0	1	1	2.78319
Degree of homogeneity of the yield function											
a											
12											

The increment of the effective plastic strain and the updated stress state are calculated after every iteration as follows:

$$\triangle\bar{\varepsilon}_{p(k+1)} = \triangle\bar{\varepsilon}_{p(k)} + \delta\bar{\varepsilon}_{p(k)} \tag{31}$$

$$\boldsymbol{\sigma}^{n+1}_{(k+1)} = \boldsymbol{\sigma}^{n+1}_{(k)} - \mathbf{L} : \left(\frac{\partial\bar{\sigma}^{n+1}}{\partial\boldsymbol{\sigma}^{n+1}}\right)_{(k)} \delta\bar{\varepsilon}_{p(k)} \tag{32}$$

The iterative procedure is performed until $f^{n+1}_{(k+1)}$ is lower than a user-defined tolerance. Then, the corresponding stress state is accepted as the current stress state. Note that the convex cutting-plane algorithm requires to obtain the first order yield function gradients (i.e. the first derivative of the effective stress with respect to the components of the stress tensor) to determine the increment of the effective plastic strain.

3.2. Implicit backward-Euler algorithm

We rewrite the yield condition and the flow rule as:

$$f^{n+1} = \bar{\sigma}^{n+1} - \sigma_Y^{n+1} = 0 \tag{27 revisited}$$

$$\mathbf{g}^{n+1} = \triangle\boldsymbol{\varepsilon}_p - \triangle\bar{\varepsilon}_p \frac{\partial\bar{\sigma}^{n+1}}{\partial\boldsymbol{\sigma}^{n+1}} = 0 \tag{33}$$

These expressions are non-linear algebraic equations in $\triangle\bar{\varepsilon}_p$ which can be solved using an iterative Newton-Raphson procedure. For that task, the previous expressions are linearized as follows:

$$f^{n+1}_{(k+1)} \approx f^{n+1}_{(k)} + \left(\frac{\partial f}{\partial\bar{\sigma}^{n+1}}\frac{\partial\bar{\sigma}^{n+1}}{\partial\boldsymbol{\sigma}^{n+1}}\frac{\partial\boldsymbol{\sigma}^{n+1}}{\partial\triangle\bar{\varepsilon}_p}\right)_{(k)} \delta\bar{\varepsilon}_{p(k)}$$
$$+ \left(\frac{\partial f}{\partial\sigma_Y^{n+1}}\frac{\partial\sigma_Y^{n+1}}{\partial\bar{\varepsilon}_p^{n+1}}\frac{\partial\bar{\varepsilon}_p^{n+1}}{\partial\triangle\bar{\varepsilon}_p}\right)_{(k)} \delta\bar{\varepsilon}_{p(k)} = 0 \tag{28 revisited}$$

$$\mathbf{g}^{n+1}_{(k+1)} \approx \mathbf{g}^{n+1}_{(k)} + \left(\frac{\partial\mathbf{g}}{\partial\triangle\boldsymbol{\varepsilon}_p}\frac{\partial\triangle\boldsymbol{\varepsilon}_p}{\partial\boldsymbol{\varepsilon}_p^{n+1}}\frac{\partial\boldsymbol{\varepsilon}_p^{n+1}}{\partial\triangle\bar{\varepsilon}_p}\right)_{(k)} \delta\bar{\varepsilon}_{p(k)}$$
$$+ \left(\frac{\partial\mathbf{g}}{\partial\boldsymbol{\sigma}^{n+1}}\frac{\partial\boldsymbol{\sigma}^{n+1}}{\partial\triangle\bar{\varepsilon}_p}\right)_{(k)} \delta\bar{\varepsilon}_{p(k)} + \left(\frac{\partial\mathbf{g}}{\partial\triangle\bar{\varepsilon}_p}\right)_{(k)} \delta\bar{\varepsilon}_{p(k)} = 0 \tag{34}$$

where

$$\frac{\partial f}{\partial\bar{\sigma}^{n+1}} = 1$$
$$\frac{\partial f}{\partial\sigma_Y^{n+1}} = -1, \qquad \frac{\partial\bar{\varepsilon}_p^{n+1}}{\partial\triangle\bar{\varepsilon}_p} = 1 \tag{29 revisited}$$

and

$$\frac{\partial\mathbf{g}}{\partial\triangle\boldsymbol{\varepsilon}_p} = \mathbf{I}, \qquad \frac{\partial\triangle\boldsymbol{\varepsilon}_p}{\partial\boldsymbol{\varepsilon}_p^{n+1}} = \mathbf{I}, \qquad \frac{\partial\boldsymbol{\varepsilon}_p^{n+1}}{\partial\triangle\bar{\varepsilon}_p} = -\mathbf{L}^{-1} : \frac{\partial\boldsymbol{\sigma}^{n+1}}{\partial\triangle\bar{\varepsilon}_p}$$
$$\frac{\partial\mathbf{g}}{\partial\boldsymbol{\sigma}^{n+1}} = -\triangle\bar{\varepsilon}_p \frac{\partial^2\bar{\sigma}^{n+1}}{\partial\boldsymbol{\sigma}^{n+1}\partial\boldsymbol{\sigma}^{n+1}} \tag{35}$$
$$\frac{\partial\mathbf{g}}{\partial\triangle\bar{\varepsilon}_p} = -\frac{\partial\bar{\sigma}^{n+1}}{\partial\boldsymbol{\sigma}^{n+1}}$$

where $\mathbf{I}$ is the unit fourth-order tensor.

From equation (34), we obtain:

$$\left(\frac{\partial\boldsymbol{\sigma}^{n+1}}{\partial\triangle\bar{\varepsilon}_p}\right)_{(k)} \delta\bar{\varepsilon}_{p(k)} = -\mathbf{E}^{n+1}_{(k)}\left(\mathbf{g}^{n+1}_{(k)} + \left(\frac{\partial\bar{\sigma}^{n+1}}{\partial\boldsymbol{\sigma}^{n+1}}\right)_{(k)} \delta\bar{\varepsilon}_{p(k)}\right) \tag{36}$$

where

$$\mathbf{E}^{n+1}_{(k)} = \left(\mathbf{L}^{-1} + \triangle\bar{\varepsilon}_{p(k)}\left(\frac{\partial^2\bar{\sigma}^{n+1}}{\partial\boldsymbol{\sigma}^{n+1}\partial\boldsymbol{\sigma}^{n+1}}\right)_{(k)}\right)^{-1} \tag{37}$$

Inserting equation (36) into equation (28), we obtain:

$$\delta\bar{\varepsilon}_{p(k)} = \left.\frac{f - \frac{\partial\bar{\sigma}}{\partial\boldsymbol{\sigma}} : \mathbf{E} : \mathbf{g}}{\frac{\partial\bar{\sigma}}{\partial\boldsymbol{\sigma}} : \mathbf{E} : \frac{\partial\bar{\sigma}}{\partial\boldsymbol{\sigma}} + \frac{\partial\sigma_Y}{\partial\bar{\varepsilon}_p}}\right|_{\bullet^{n+1}_{(k)}} \tag{38}$$

The increment of the effective plastic strain and the updated stress state are calculated after every iteration as follows:

$$\triangle\bar{\varepsilon}_{p(k+1)} = \triangle\bar{\varepsilon}_{p(k)} + \delta\bar{\varepsilon}_{p(k)} \tag{31 revisited}$$

$$\boldsymbol{\sigma}^{n+1}_{(k+1)} = \boldsymbol{\sigma}^{n+1}_{(k)} - \mathbf{E}^{n+1}_{(k)}\left(\mathbf{g}^{n+1}_{(k)} + \left(\frac{\partial\bar{\sigma}^{n+1}}{\partial\boldsymbol{\sigma}^{n+1}}\right)_{(k)} \delta\bar{\varepsilon}_{p(k)}\right) \tag{39}$$

The iterative procedure is performed until $f^{n+1}_{(k+1)}$ and $\mathbf{g}^{n+1}_{(k+1)}$ are lower than a user-defined tolerance. Then, the corresponding stress state is accepted as the current stress state. Note that the implicit backward-Euler algorithm requires to obtain the first and second order yield function gradients (i.e. the first and second derivatives of the effective stress with respect to the components of the stress tensor) to determine the increment of the effective plastic strain.

4. Algorithmic tangent modulus

In this section, we derive the general expression of the algorithmic tangent modulus, a critical factor in the UMAT implementation of the constitutive models to preserve the quadratic rate of asymptotic convergence of the iterative Newton-Raphson procedure (see equations (27) and (33)). See, for instance, Yoon et al. [46] and Yoon et al. [39] for additional details.

The stress at time $n+1$ is:

$$\boldsymbol{\sigma}^{n+1} = \boldsymbol{\sigma}^{n} + \mathbf{L} : \triangle\boldsymbol{\varepsilon} - \triangle\bar{\varepsilon}_p\mathbf{L} : \frac{\partial\bar{\sigma}^{n+1}}{\partial\boldsymbol{\sigma}^{n+1}} \tag{40}$$

Differentiation of previous expression leads to:

$$\delta\boldsymbol{\sigma} = \mathbf{L}\left(\delta\boldsymbol{\varepsilon} - \frac{\partial\bar{\sigma}^{n+1}}{\partial\boldsymbol{\sigma}^{n+1}}\delta\bar{\varepsilon}_p - \triangle\bar{\varepsilon}_p\frac{\partial^2\bar{\sigma}^{n+1}}{\partial\boldsymbol{\sigma}^{n+1}\partial\boldsymbol{\sigma}^{n+1}}\delta\boldsymbol{\sigma}\right) \tag{41}$$

which can be recast into:

$$\delta\boldsymbol{\sigma} = \bar{\mathbf{L}}\left(\delta\boldsymbol{\varepsilon} - \frac{\partial\bar{\sigma}^{n+1}}{\partial\boldsymbol{\sigma}^{n+1}}\delta\bar{\varepsilon}_p\right) \tag{42}$$

where:

$$\bar{\mathbf{L}} = \left(\mathbf{L}^{-1} + \triangle \bar{\varepsilon}_p \frac{\partial^2 \bar{\sigma}^{n+1}}{\partial \boldsymbol{\sigma}^{n+1} \partial \boldsymbol{\sigma}^{n+1}} \right)^{-1} \tag{43}$$

Differentiation of the consistency condition, equation (27), leads to:

$$\delta f = \left(\frac{\partial f}{\partial \bar{\sigma}^{n+1}} \frac{\partial \bar{\sigma}^{n+1}}{\partial \boldsymbol{\sigma}^{n+1}} \right) \delta \boldsymbol{\sigma} + \left(\frac{\partial f}{\partial \bar{\sigma}_Y^{n+1}} \frac{\partial \bar{\sigma}_Y^{n+1}}{\partial \bar{\varepsilon}_p^{n+1}} \frac{\partial \bar{\varepsilon}_p^{n+1}}{\partial \triangle \bar{\varepsilon}_p} \right) \delta \bar{\varepsilon}_p = 0 \tag{44}$$

Substituting equation (42) into equation (44) gives the following relation:

$$\delta \bar{\varepsilon}_p = \frac{\frac{\partial \bar{\sigma}^{n+1}}{\partial \boldsymbol{\sigma}^{n+1}} : \bar{\mathbf{L}} : \delta \boldsymbol{\varepsilon}}{\frac{\partial \bar{\sigma}^{n+1}}{\partial \boldsymbol{\sigma}^{n+1}} : \bar{\mathbf{L}} : \frac{\partial \bar{\sigma}^{n+1}}{\partial \boldsymbol{\sigma}^{n+1}} + \frac{\partial \sigma_Y^{n+1}}{\partial \bar{\varepsilon}_p^{n+1}}} \tag{45}$$

Inserting equation (45) into equation (42) yields:

$$\delta \boldsymbol{\sigma} = \bar{\mathbf{L}}^{\text{ep}} : \delta \boldsymbol{\varepsilon} \tag{46}$$

where:

$$\bar{\mathbf{L}}^{\text{ep}} = \left(\bar{\mathbf{L}} - \frac{\bar{\mathbf{L}} : \frac{\partial \bar{\sigma}^{n+1}}{\partial \boldsymbol{\sigma}^{n+1}} \otimes \bar{\mathbf{L}} : \frac{\partial \bar{\sigma}^{n+1}}{\partial \boldsymbol{\sigma}^{n+1}}}{\frac{\partial \bar{\sigma}^{n+1}}{\partial \boldsymbol{\sigma}^{n+1}} : \bar{\mathbf{L}} : \frac{\partial \bar{\sigma}^{n+1}}{\partial \boldsymbol{\sigma}^{n+1}} + \frac{\partial \sigma_Y^{n+1}}{\partial \bar{\varepsilon}_p^{n+1}}} \right) \tag{47}$$

is the algorithmic tangent modulus. Note that we need to obtain the first and second order yield function gradients to calculate the algorithmic tangent modulus.

The idea of giving details on the formulation of the constitutive models in Section 2, and on the integration algorithms in Sections 3 and 4, stems from our goal of providing a self-contained manuscript, that it is easy to follow and fully reproducible.

5. Numerical approximations for the stress derivatives

This section presents a numerical approximation of the first and second derivatives of the effective stress with respect to the components of the stress tensor. This is a simple alternative to the analytical derivatives, which are given in Appendix A, that reduces the computational time without impairing the accuracy of the finite element calculations (see Section 7). As mentioned before, these derivatives are required for the integration of the constitutive equations, namely, for the calculation of the effective plastic strain increment in the convex cutting-plane and the implicit backward-Euler algorithms, equations (30) and (38), and for the calculation of the algorithmic tangent modulus, see equation (47).

5.1. First derivative approximation

The interpolation polynomial of Lagrange, for a set of $k+1$ data points $(x_0, h(x_0))$, …,$(x_j, h(x_j))$, …,$(x_k, h(x_k))$, where no two x_j are the same, is:

$$h(x) \approx \sum_{j=0}^{k} h(x_j) L_j(x) \tag{48}$$

where

$$L_j(x) = \prod_{m=0, m\neq j}^{k} \frac{x - x_m}{x_j - x_m} = \frac{x - x_0}{x_j - x_0} \cdots \frac{x - x_{j-1}}{x_j - x_{j-1}} \frac{x - x_{j+1}}{x_j - x_{j+1}} \cdots \frac{x - x_k}{x_j - x_k} \tag{49}$$

For a set of 3 *equally-spaced* data points $(x_0, h(x_0)), (x_1, h(x_1)), (x_2, h(x_2))$ which fulfill the conditions $x_0 = x_1 - a$ and $x_2 = x_1 + a$, the derivative of equation (48) leads to:

$$\left. \frac{\partial h(x)}{\partial x} \right|_{x_1} \approx \frac{h(x_2) - h(x_0)}{2a} \tag{50}$$

Particularization of previous expression for the derivative of the effective stress with respect to the stress components leads to:

$$\frac{\partial \bar{\sigma}}{\partial \sigma_{ij}} \approx \frac{\bar{\sigma}(\sigma_{ij} + \Delta\sigma_{ij}) - \bar{\sigma}(\sigma_{ij} - \Delta\sigma_{ij})}{2\Delta\sigma_{ij}} \tag{51}$$

Notice that previous expression is equivalent to the central difference scheme used by Choi and Yoon [1]; see Appendix B, and different from the forward difference scheme reported in Appendix A.2 of Banabic et al. [47]; Appendix C of Barlat et al. [2] and Aretz [41].

5.2. Second derivatives approximation

The first three terms of the Taylor series expansion for approximating $h(x_1 + a)$ and $h(x_1 - a)$ about x_1 are:

$$h(x)|_{x_1+a} \approx h(x)|_{x_1} + \left. \frac{\partial h(x)}{\partial x} \right|_{x_1} a + \frac{1}{2} \left. \frac{\partial^2 h(x)}{\partial x \partial x} \right|_{x_1} a^2 \tag{52}$$

and

$$h(x)|_{x_1-a} \approx h(x)|_{x_1} - \left. \frac{\partial h(x)}{\partial x} \right|_{x_1} a + \frac{1}{2} \left. \frac{\partial^2 h(x)}{\partial x \partial x} \right|_{x_1} a^2 \tag{53}$$

Adding equations (52) and (53) we obtain:

$$\left. \frac{\partial^2 h(x)}{\partial x \partial x} \right|_{x_1} \approx \frac{h(x_1 - a) - 2h(x_1) + h(x_1 + a)}{a^2} \tag{54}$$

Particularization of previous expression for the second derivative of $\bar{\sigma}$ with respect to the stress components when $ij = kl$ leads to:

$$\frac{\partial^2 \bar{\sigma}}{\partial \sigma_{ij} \partial \sigma_{ij}} \approx \frac{\bar{\sigma}(\sigma_{ij} - \Delta\sigma_{ij}) - 2\bar{\sigma} + \bar{\sigma}(\sigma_{ij} + \Delta\sigma_{ij})}{\Delta\sigma_{ij}^2} \tag{55}$$

Notice that previous expression is the same used by Choi and Yoon [1]; see Appendix B.

Moreover, the first three terms of the Taylor series expansion for approximating $h(x_1 + a, y_1 + a)$ and $h(x_1 - a, y_1 - a)$ about (x_1, y_1) are:

$$\begin{aligned} h(x,y)|_{(x_1+a,y_1+a)} \approx & h(x,y)|_{(x_1,y_1)} + \left. \frac{\partial h(x,y)}{\partial x} \right|_{(x_1,y_1)} a + \left. \frac{\partial h(x,y)}{\partial y} \right|_{(x_1,y_1)} a \\ & + \frac{1}{2} \left. \frac{\partial h^2(x,y)}{\partial x \partial x} \right|_{(x_1,y_1)} a^2 + \left. \frac{\partial h^2(x,y)}{\partial x \partial y} \right|_{(x_1,y_1)} a^2 \\ & + \frac{1}{2} \left. \frac{\partial h^2(x,y)}{\partial y \partial y} \right|_{(x_1,y_1)} a^2 \end{aligned} \tag{56}$$

and

$$\begin{aligned} h(x,y)|_{(x_1-a,y_1-a)} \approx & h(x,y)|_{(x_1,y_1)} - \left. \frac{\partial h(x,y)}{\partial x} \right|_{(x_1,y_1)} a - \left. \frac{\partial h(x,y)}{\partial y} \right|_{(x_1,y_1)} a \\ & + \frac{1}{2} \left. \frac{\partial h^2(x,y)}{\partial x \partial x} \right|_{(x_1,y_1)} a^2 + \left. \frac{\partial h^2(x,y)}{\partial x \partial y} \right|_{(x_1,y_1)} a^2 \\ & + \frac{1}{2} \left. \frac{\partial h^2(x,y)}{\partial y \partial y} \right|_{(x_1,y_1)} a^2 \end{aligned} \tag{57}$$

Adding equations (56) and (57) leads to:

$$\begin{aligned} \left. \frac{\partial h^2(x,y)}{\partial x \partial y} \right|_{(x_1,y_1)} \approx & \frac{h(x_1 - a, y_1 - a) - 2h(x_1, y_1) + h(x_1 + a, y_1 + h)}{2a^2} \\ & - \frac{1}{2} \left. \frac{\partial h^2(x,y)}{\partial x \partial x} \right|_{(x_1,y_1)} - \frac{1}{2} \left. \frac{\partial h^2(x,y)}{\partial y \partial y} \right|_{(x_1,y_1)} \end{aligned} \tag{58}$$

Particularizing previous expression for the second derivative of $\bar{\sigma}$ with respect to the stress components when $ij \neq kl$ leads to:

$$\frac{\partial^2\bar{\sigma}}{\partial\sigma_{ij}\partial\sigma_{kl}} \approx \frac{\bar{\sigma}(\sigma_{ij}-\Delta\sigma_{ij},\sigma_{kl}-\Delta\sigma_{kl})-2\bar{\sigma}+\bar{\sigma}(\sigma_{ij}+\Delta\sigma_{ij},\sigma_{kl}+\Delta\sigma_{kl})}{2\Delta\sigma_{ij}\Delta\sigma_{kl}} - \frac{1}{2}\frac{\partial^2\bar{\sigma}}{\partial\sigma_{ij}\partial\sigma_{ij}} - \frac{1}{2}\frac{\partial^2\bar{\sigma}}{\partial\sigma_{kl}\partial\sigma_{kl}} \tag{59}$$

where $\Delta\sigma_{ij} = \Delta\sigma_{kl}$. Notice that previous expression is different from the formulation used by Choi and Yoon [1]; see Appendix B, and thus an original contribution of this paper. All the calculations shown in Section 7 are performed with $\Delta\sigma_{ij} = \Delta\sigma_{kl} = 0.01$ MPa. Nevertheless, we also carried out simulations with $\Delta\sigma_{ij} = \Delta\sigma_{kl} = 0.001$ and 0.0001 MPa and the differences in the numerical results (stress and strain fields in the specimen) were negligible. Moreover, we have checked that the relative error of the numerical derivatives with respect to their analytical counterparts, for the three stress steps $\Delta\sigma_{ij} = \Delta\sigma_{kl} = 0.1$, 0.01 and 0.001 MPa, is less than 10^{-8} for all the calculations performed in this work, thus having negligible influence in the finite element results (see Section 7.1).

Notice that the simple form of equations (51), (55) and (59), in comparison with the analytical derivatives shown in Appendix A, greatly facilitates the implementation of the constitutive models in finite element codes. It was also pointed out by Barlat et al. [2] that the singularities of the analytical derivatives shown in Appendix A.4 can be avoided by using numerical approximation of the yield function gradients. As it will be shown in Section 7, using the numerical approximation of the second derivative leads to a significant decrease of the computational time in simulations performed with UMAT subroutines in ABAQUS/Standard implicit calculations. In addition, the computational cost of the numerical approximations proposed in this paper is smaller than that of the numerical differentiation scheme used by Choi and Yoon [1]; see Section 7.2. The comparison performed in Section 7 between the computational efficiency of the numerical differentiation schemed used in this paper and the approach of Choi and Yoon [1] is a novel aspect of this manuscript. In this regard, note that Choi and Yoon[1] only performed small scale simulations: single element calculations to evaluate the accuracy of the numerical derivatives, and deep drawing simulations where the blank is modeled with a single layer of shell elements to check the number of ears predicted by the various constitutive models investigated. The larger scale calculations presented in Section 7, with finite element models including tens of thousands of elements, are an original contribution of this paper.

6. Finite element models

This section presents the finite element models developed in ABAQUS [48] to carry out cylindrical cup deep drawing test calculations (Section 6.1) and simulations of dynamic necking localization under plane strain tension (Section 6.2) with AA 2090-T3 specimens modeled with the three yield criteria presented in Section 2.

6.1. Cup deep drawing

Fig. 1 shows a schematic representation of the cylindrical cup deep drawing process. The specific tools and blank dimensions are given in Table 5.

Taking advantage of the problem symmetry and the orthotropy of the material, only a quarter section of the cup is analyzed. The loading condition is a prescribed constant velocity imposed to the punch of 0.4 m/s. Similarly to Aretz and Barlat [4]; a blank-holder force of 5.5 kN for the quarter model (corresponding to approximately one percent of the initial yield stress of the material in the rolling direction) has been applied during the simulations. The friction is modeled with Coulomb's law, with a friction coefficient equal to 0.1 for all contact surfaces [37].

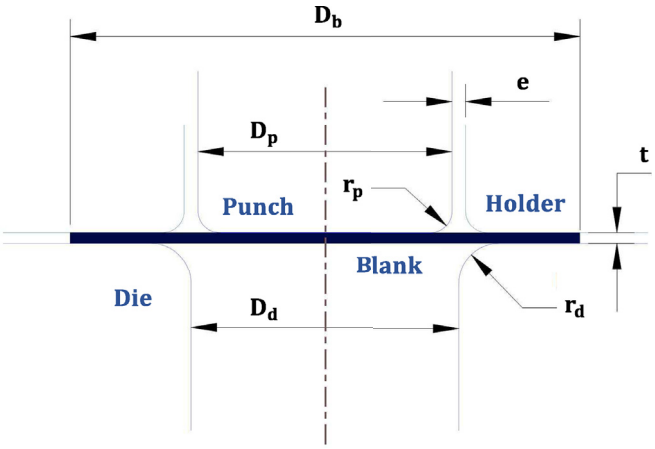

Fig. 1. Tools and blank geometries for cylindrical cup deep drawing. This figure is adapted from Yoon et al. [39,46].

Punch, holder and die are modeled as rigid solids. Moreover, the blank has been meshed with tri-linear solid elements with 8-nodes (C3D8 in ABAQUS notation). We have used 5 different meshes (mesh 1, …,mesh 5) in which the number of elements trough the thickness increases from 1 to 5. The number of elements in each mesh is: 5915, 11830, 17745, 23660 and 29575. The goal is to illustrate the computational time saving obtained with the numerical approximation of the stress derivatives as the number of elements of the model increases. The mesh design of the blank with 5 elements through the thickness is shown in Fig. 2.

To the authors' knowledge, there are just few relevant papers using several solid elements through the thickness of the blank to simulate deep drawing of circular cups [49]. Deep drawing calculations are usually performed with a single solid element through the thickness of the specimen, notably when advanced constitutive models are used (see Yoon et al. [37]; Vladimirov et al. [50]; Shutov et al. [51], often with the aim of limiting the computational time. Shell type elements have also been used in several works [1,4,39,52]. As mentioned before, the cylindrical cup deep drawing test calculations performed in this paper with finite element models that include tens of thousands of elements, are an original contribution of this work.

6.2. Plane strain tension

This section presents the 2D finite element model used to simulate dynamic necking localization under plane strain tension. Material points are referred to using a Cartesian coordinate system with positions in the reference configuration denoted as (X, Y). The specimen is under plane strain constraint in the out-of-plane direction. The origin of coordinates is located in the center of mass of the specimen, see Fig. 3. We use the same finite element model as N'souglo et al. [42] who, following the earlier work of Xue et al. [53]; modeled a plate subjected to plane strain tension, and with geometric periodic perturbations, as an array of unit cells with sinusoidal spatial imperfections given by the following expression:

$$h = h^0 - \delta\left[1+\cos\left(\frac{2\pi X}{L^0}\right)\right] \tag{60}$$

where h is the perturbed thickness of the unit cell and δ is the amplitude of the imperfection. Moreover, L^0 and h^0 are the initial length and the unperturbed thickness of the unit cell, respectively (see Fig. 3). Due to the symmetry of the problem, only a quarter of the unit cell is analyzed, see Fig. 3. For all the calculations presented in Section 7.2, the rolling direction is aligned with the X axis. Finite element simulations will be conducted for several normalized cell lengths varying within the range $0.5 < \frac{L^0}{h^0} \leq 6$, with $\Delta = \frac{2\delta}{h^0} = 0.2\%$ and $h^0 = 2$ mm. Hereinafter,

Table 5
Tools and blank dimensions for the cup deep drawing test. Data after Yoon et al. [37].

D_p (mm)	D_d (mm)	D_b (mm)	r_p (mm)	r_d (mm)	e (mm)	t (mm)
97.46	101.48	158.76	12.7	12.7	2.7	1.6

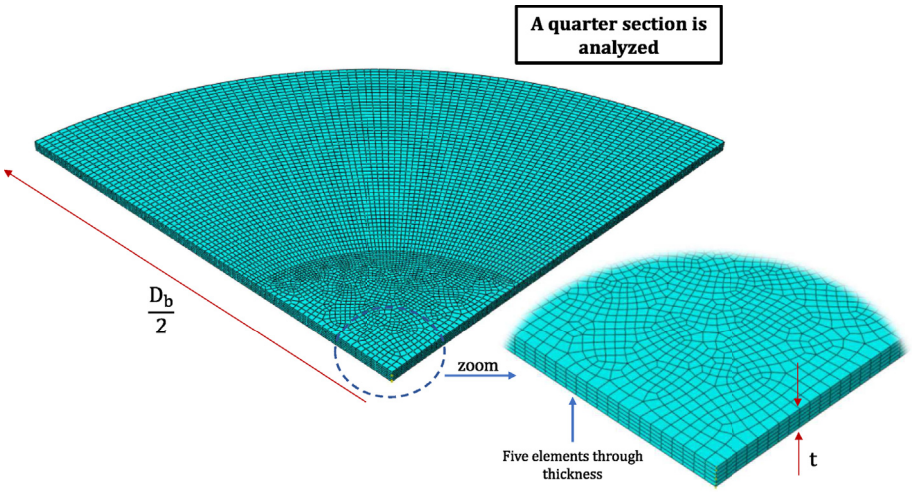

Fig. 2. Blank mesh used in the finite element simulations. Five elements through the thickness of the sheet. Total number of elements: 29575.

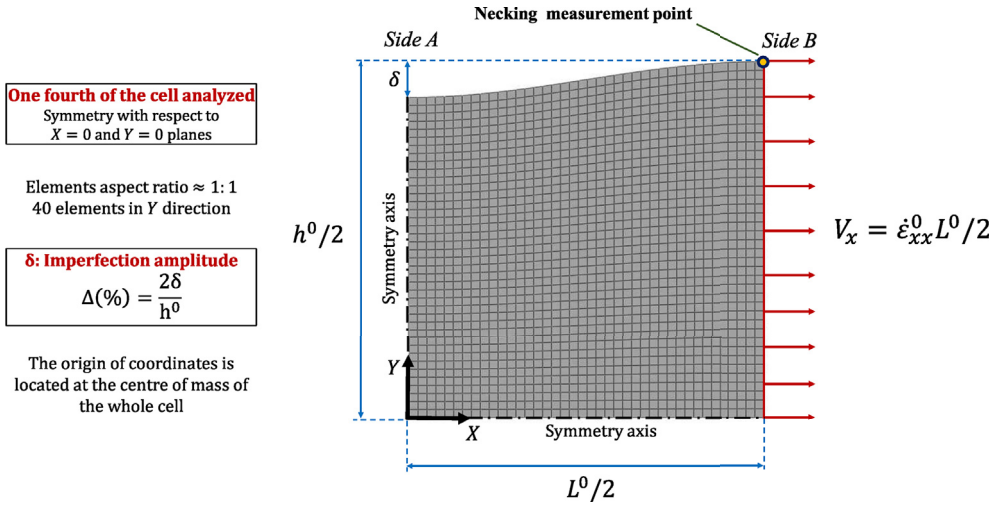

Fig. 3. Finite element model. Mesh and boundary conditions. A large imperfection amplitude has been shown in the figure for better illustration of the geometric perturbation. This figure is taken from N'souglo et al. [42]. The specimen is under plane strain constraint in the out-of-plane direction.

the normalized cell length will be also referred to as cell size. Note that the spatial imperfection is imposed on lines $X = constant$ which is the orientation naturally selected by the material to trigger a neck under plane strain tension when the orthotropy and the loading are codirectional. The initial and boundary conditions used in the finite element model are:

$$V_x(X,Y,0) = \dot{\varepsilon}^0_{xx} X$$
$$V_y(X,Y,0) = -\dot{\varepsilon}^0_{xx} Y \tag{61}$$

and

$$U_x(0,Y,t) = 0, \qquad U_y(X,0,t) = 0$$
$$V_x\left(L^0/2,Y,t\right) = \dot{\varepsilon}^0_{xx} L^0/2 \tag{62}$$

where $\dot{\varepsilon}^0_{xx}$ is the initial strain rate imposed on the loading direction.

The finite element model is meshed with four-node bilinear plane strain elements with reduced integration and hourglass control (CPE4R in ABAQUS notation), with initial dimensions $\approx 25 \times 25\ \mu m^2$.

7. Sample results

In this section, we present sample finite elements results for deep drawing (Section 7.1) and dynamic necking localization under plane strain tension (Section 7.2). We have performed implicit and explicit finite element simulations using UMAT and VUMAT subroutines, respectively, with the analytical derivatives of Appendix A, the numerical approximations of Section 5, and the numerical differentiation scheme developed by Choi and Yoon [1]; which is shown in Appendix B. Note that we provide access to the UMAT and VUMAT codes developed in this paper. Recall that the convex cutting-plane

Table 6
CPU time for cup deep drawing finite element simulations performed with the three yield criteria presented in Section 2. The results obtained with the analytical derivatives of Appendix A (denoted with -A) and the numerical approximations of Section 5 (denoted with –N) are compared. The simulations have been performed using a dynamic implicit analysis in ABAQUS/Standard and UMAT subroutines for the yield functions implementation.

CPU time (units in kiloseconds)

	Yld2004-18p-A	Yld2004-18p-N	CPB06ex2-A	CPB06ex2-N	Yld2011-27p-A	Yld2011-27p-N
1 Element	128.752	60.520	107.991	61.940	132.977	62.957
2 Elements	211.607	80.443	184.322	87.444	229.964	90.574
3 Elements	319.536	109.008	265.738	118.439	327.210	120.531
4 Elements	411.566	132.924	355.614	159.813	435.562	154.776
5 Elements	544.324	174.803	448.508	205.446	567.211	199.222

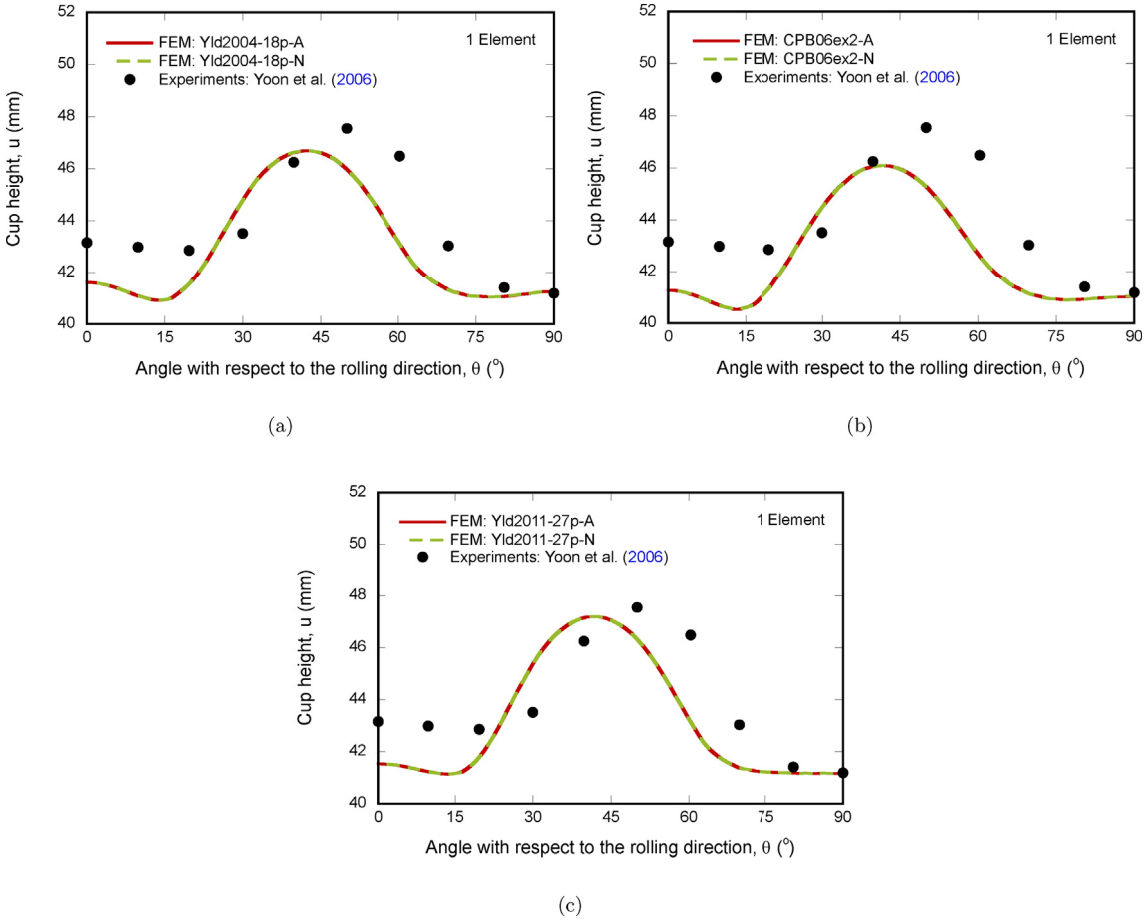

Fig. 4. Comparison between finite element simulations (FEM) and experimental results. Cup height u as a function of the angle with respect to the rolling direction θ. The experimental data are taken from Yoon et al. [37]. The finite elements results are obtained with the analytical derivatives of Appendix A (denoted with -A) and the numerical approximations of Section 5 (denoted with –N). The calculations are performed with 1 element trough the thickness of the sheet. (a) Yld2004-18p-A and Yld2004-18p-N. (b) CPB06ex2-A and CPB06ex2-N. (c) Yld2011-27p-A and Yld2011-27p-N. The simulations have been performed using a dynamic implicit analysis in ABAQUS/Standard and UMAT subroutines for the yield functions implementation.

algorithm used to code the VUMAT involves only the first derivative of the yield function gradients, which takes the same form in the numerical differentiation scheme developed in Section 5 and in the formulation proposed by Choi and Yoon [1]; see Appendix B. All the calculations have been performed with a personal computer using a single CPU with the following features: Intel(R) Core(TM) *i7 − 8550U* CPU @1.80 GHz1.99GHZ.

7.1. Cup deep drawing

This section presents the results corresponding to the cup deep drawing finite element calculations. The simulations have been performed using a dynamic implicit analysis in ABAQUS/Standard and UMAT subroutines for the yield functions implementation. The calculations are terminated when the displacement of the punch reaches 60 mm, so that we make sure that the deep drawing operation has been completed (additional punch displacement does not lead to further specimen deformation, see Figs. 6 and 7). Table 6 shows the CPU times corresponding to the simulations performed with the three yield criteria, using five different meshes for the blank in which the number of elements trough the thickness varies from 1 to 5 (see Section 6.1). The CPU times obtained with the analytical derivatives of Appendix A (denoted

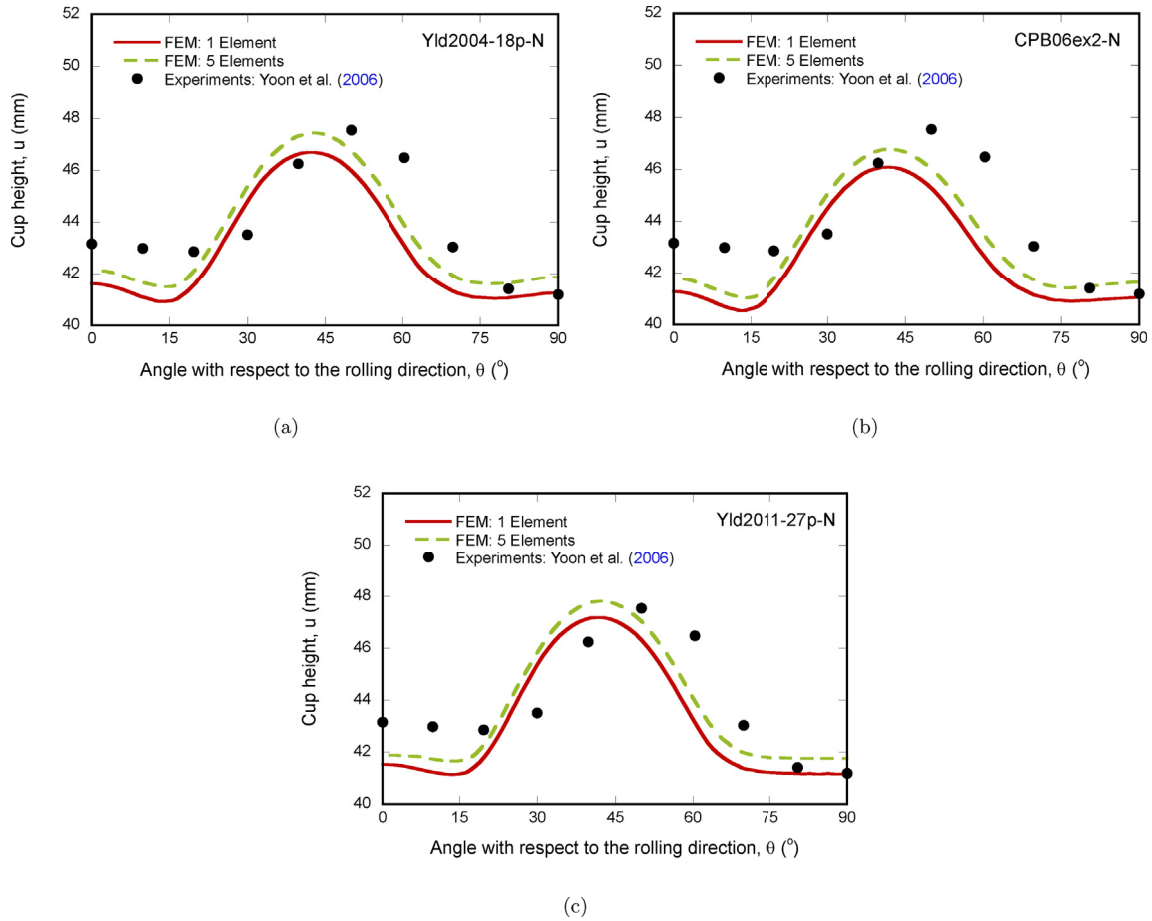

Fig. 5. Comparison between finite element simulations (FEM) and experimental results. Cup height u as a function of the angle with respect to the rolling direction θ. The experimental data are taken from Yoon et al. [37]. The finite elements results are obtained with the numerical approximations of Section 5 (denoted with –N). The calculations are performed with 1 element and 5 elements through the thickness of the sheet. (a) Yld2004-18p-N. (b) CPB06ex2-N. (c) Yld2011-27p-N. The simulations have been performed using a dynamic implicit analysis in ABAQUS/Standard and UMAT subroutines for the yield functions implementation.

with -A) and the numerical approximations of Section 5 (denoted with –N) are compared. Using the numerical approximations leads to a significant decrease of the computational time for the three yield criteria, and this decrease is greater as the number of elements in the mesh increases. This is an original result of this paper. Namely, for the Yld2004-18p criterion, the CPU times obtained using the numerical approximations of the yield function gradients are $\approx 47\%$ and $\approx 32\%$ of those obtained using the analytical derivatives for the meshes with 1 and 5 elements trough the thickness, respectively. For the CPB06ex2 model these percentages are $\approx 57\%$ and $\approx 46\%$ (i.e. smaller computational time decrease than in the case of Yld2004-18p criterion), and for the Yld2011-27p model they are $\approx 47\%$ and $\approx 35\%$, respectively. It becomes apparent that the decrease of the computational time using the numerical approximations enables to perform larger scale ABAQUS/Standard calculations. For instance, the CPU time for Yld2004-18p-N with 5 elements through the thickness is *only* 1.35 times the CPU time corresponding to Yld2004-18p-A with 1 element trough the thickness.

A key point is that, despite the significant reduction in computational time, the results are practically the same using the analytical derivatives and the numerical approximations of the yield functions gradients. Fig. 4 shows finite element results for the cup height u as a function of the angle with respect to the rolling direction θ. The cup height is measured when the displacement of the punch reaches 60 mm (when the simulation is terminated). The calculations are performed with 1 element trough the thickness. The finite elements results correspond to: (a) Yld2004-18p-A and Yld2004-18p-N, (b) CPB06ex2-A and CPB06ex2-N and (c) Yld2011-27p-A and Yld2011-27p-N (same notation used in Table 6). The $u-\theta$ curves obtained with the analytical derivatives and the numerical approximations are virtually on top of each other (we have checked that this agreement occurs for the 5 meshes investigated). Moreover, note that we also compare the finite element results with the experimental data reported by Yoon et al. [37] for AA 2090-T3. The qualitative agreement between the predictions of the three yield criteria and the experiments is satisfactory (note that Yoon et al. [37] already compared these experiments with the predictions of the Yld2004-18p-A criterion), with a maximum of the cup height for an intermediate value of θ, and minima near the rolling and transverse directions, with the cup height being greater for $\theta = 0°$ than for $\theta = 90°$. However, the three models show quantitative differences with the experiments, especially in the prediction of the cup height for $\theta = 0°$, and in the maximum value of u for $\theta \approx 50°$. According to Yoon et al. [37]; the discrepancies between the numerical predictions and the experiments could be partially attributed to the fact that the center of the blank was not aligned properly with the centers of the die and the punch during the drawing test.

Fig. 5 shows the comparison of the cup height results obtained with the numerical approximation of the yield function gradients of Section 5 for the meshes with 1 and 5 elements trough the thickness of the sheet, for the three yield criteria: (a) Yld2004-18p-N, (b) CPB06ex2-N and (c) Yld2011-27p-N. Note that the results with 1 element trough the thickness were already presented in Fig. 4. The increase in the number of elements shifts upwards the $u-\theta$ curves, such that the cup height, for any angle θ, is ≈ 1 mm greater when 5 elements trough the thickness are

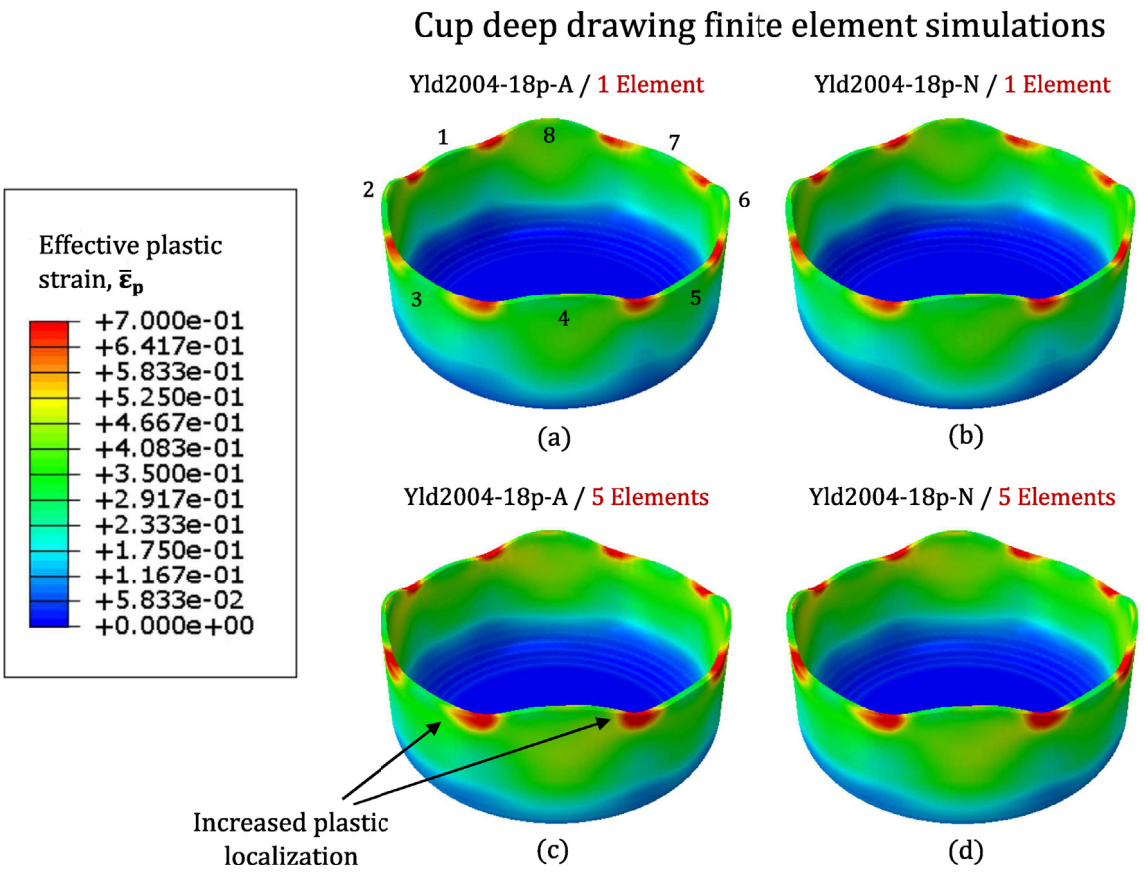

Fig. 6. Finite element simulations. Cup deep drawing calculations. Contours of effective plastic strain $\bar{\varepsilon}_p$ corresponding to calculations performed with Yld2004-18p yield criterion. Comparison between results obtained with the analytical derivatives of Appendix A (denoted with -A) and the numerical approximations of Section 5 (denoted with –N). Calculations performed with 1 and 5 elements trough the thickness. (a) Yld2004-18p-A and 1 element trough the thickness. (b) Yld2004-18p-N and 1 element trough the thickness. (c) Yld2004-18p-A and 5 elements trough the thickness. (d) Yld2004-18p-N and 5 elements trough the thickness. The simulations have been performed using a dynamic implicit analysis in ABAQUS/Standard and UMAT subroutines for the yield function implementation.

used, leading to slightly better quantitative agreement with the experiments of Yoon et al. [37]. Moreover, increasing the number of elements generally helps to describe plastic localization phenomena, reducing the pathological mesh sensitivity obtained with rate-independent materials in problems where inertia forces are not relevant [54]. The contours of effective plastic strain presented in Fig. 6 for the Yld2004-18p criterion show a comparison between the results obtained with the analytical derivatives and the numerical approximation of the yield function gradients proposed in Section 5, for simulations performed with 1 and 5 elements trough the thickness. The contours are taken when the displacement of the punch reaches 60 mm (when the simulations are terminated). All the isocontours have the same color coding, so that effective plastic strains ranging from 0 to 0.7 correlate with a colour scale that goes from blue to red. Effective plastic strains greater than 0.7 remain red, so that the red zones in the cups correspond to areas with highly localized plastic deformation and important thinning of the thickness of the cup. These red zones, which are located between the 8 ears that develop in the cups (which are numbered in Fig. 6(a)) have greater extension for the calculations performed with 5 elements trough the thickness of the specimen, illustrating the influence of the mesh in simulating plastic localization processes (when rate-independent materials are used). As stated by Yoon et al. [37]; the Yld2004-18p criterion, unlike many other phenomenological yield functions, shows the capability of predicting more than four ears in cup drawing. Moreover, note that the contours of plastic strain for the calculations performed with the analytical derivatives and the numerical approximation of the yield function gradients proposed in Section 5 are virtually identical (compare Fig. 6(a) and (c) with Fig. 6(b) and (d), respectively). In future works, it is recommended to include strain rate and temperature effects in the evolution of the yield stress of the material, in order to develop a more comprehensive analysis on the material aspects that control plastic localization in deep drawing operations.

Fig. 7 shows contours of effective plastic strain $\bar{\varepsilon}_p$ corresponding to calculations performed with 5 elements trough the thickness of the sheet for CPB06ex2 and Yld2011-27p criteria. The color coding is the same used in Fig. 6. The results obtained with the analytical derivatives of Appendix A and the numerical approximation of the yield function gradients of Section 5 are compared: (a) CPB06ex2-A, (b) CPB06ex2-N, (c) Yld2011-27p-A and (d) Yld2011-27p-N. As for the Yld2004-18p criterion, the procedure used to calculate the stress derivatives has no influence on the plastic strain contours (compare Fig. 7(a) and (c) with Fig. 7(b) and (d), respectively). Eight ears are formed in the four calculations shown in Fig. 7, being the height of numbers 2, 4, 6 and 8 greater than the height of the other four. On the other hand, the yield criterion plays a role in the localization zones between the ears of the cup, which have slightly greater extension in the case of CPB06ex2 model (compare Fig. 7(a) and (b) with Fig. 7(c) and (d), respectively). Nevertheless, the distribution of plastic strains in the specimen is similar for both yield criteria.

7.2. Plane strain tension

This section presents the results corresponding to the dynamic plane strain tension calculations. We have performed simulations with both UMAT and VUMAT subroutines, using the numerical approximation of the yield function gradients of Section 5 and the numerical differen-

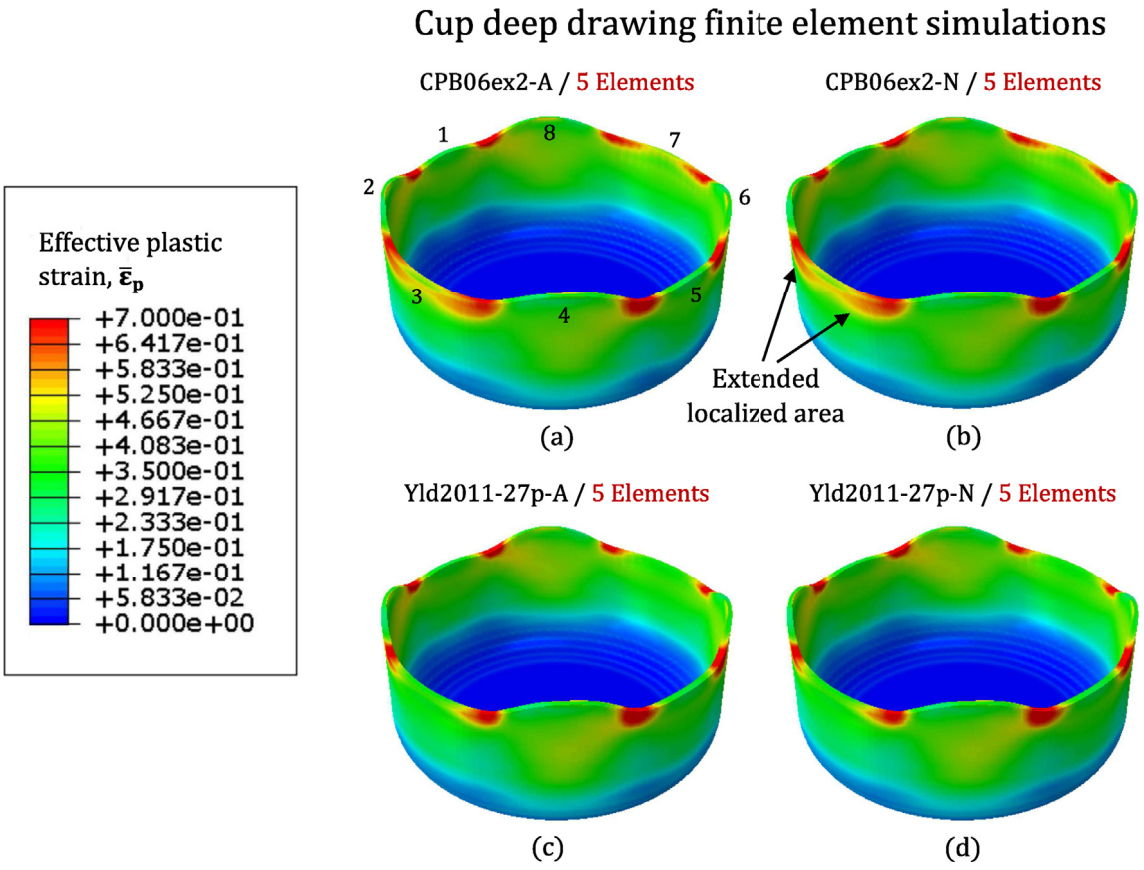

Fig. 7. Finite element simulations. Cup deep drawing calculations. Contours of effective plastic strain $\bar{\varepsilon}_p$ corresponding to calculations performed with 5 elements trough the thickness. Comparison between results obtained with the analytical derivatives of Appendix A (denoted with -A) and the numerical approximations of Section 5 (denoted with –N). (a) CPB06ex2-A. (b) CPB06ex2-N. (c) Yld2011-27p-A. (d) Yld2011-27p-N. The simulations have been performed using a dynamic implicit analysis in ABAQUS/Standard and UMAT subroutines for the yield functions implementation.

tiation scheme developed by Choi and Yoon [1]; which is shown in Appendix B. While we do not show the results for the sake of brevity, we have checked that the explicit calculations with the analytical expressions of the yield function gradients are not computationally more expensive, which brings out that the numerical approximation of the yield function gradients is computationally advantageous only if the second order yield function gradients are involved in the integration scheme (i.e. for the UMAT, as shown in Section 7.1). The calculations are carried out for two imposed initial strain rates $\dot{\varepsilon}^0_{xx} = 100\ \text{s}^{-1}$ and $10000\ \text{s}^{-1}$ (see Section 6.2). This range of strain rates is usually attained in high energy rate forming processes, such as electromagnetic and electrohydraulic forming, in which the formation of dynamic necks imposes limitations to the material formability [55,56].

Fig. 8 shows the evolution of the necking strain $\bar{\varepsilon}^{neck}$ with the cell size L^0/h^0, for dynamic implicit and explicit simulations performed for $\dot{\varepsilon}^0_{xx} = 100\ \text{s}^{-1}$ with the numerical approximation of the yield function gradients and the three yield criteria. The implicit calculations are performed with the numerical approximation of the stress derivatives of Section 5 and the numerical differentiation scheme developed by Choi and Yoon [1]; see Appendix B. Recall that explicit calculations only require the first derivative of the yield function gradients, which is the same in the scheme developed in Section 5 and in the formulation proposed by Choi and Yoon [1]. The necking strain corresponds to the effective plastic strain measured in the finite element located at the upper right corner of the thickest section of the cell (see the yellow marker in Fig. 3) when the effective plastic strain rate equals $10^{-3}\ \text{s}^{-1}$ in that specific element (similar procedure was applied in Rodríguez-Martínez et al. [57] and N'souglo et al.[42,58]). This condition indicates that plastic strain has been localized in the center of the specimen and the ends of the cell are unloaded. The necking strain decreases nonlinearly with the cell size, displaying a concave-upwards shape, with a large slope for small values of L^0/h^0, which is gradually reduced with the increase of the cell length. The large values of the necking strain for short cells are due to the stabilizing effects of stress multiaxiality, which delay necking formation [42,57,58]. The results obtained for the three yield criteria are very similar, qualitatively and quantitatively, with slightly larger necking strains for the CPB06ex2 model. However, these differences are hardly noticeable unless the $\bar{\varepsilon}^{neck} - L^0/h^0$ curves are plotted in the same graph. Still, we do not choose such representation of results because it would make the comparison between the UMAT and VUMAT results less clear. Notice that the results presented in Fig. 8 bring out that the necking strains predicted by the implicit and the explicit calculations are virtually the same. The key outcome is that the implicit analyses performed with the UMAT, using both the numerical differentiation scheme developed in this paper and the formulation of Choi and Yoon [1]; are significantly cheaper in terms of computational cost, see Table 7 (the CPU time is taken approximately when the necking condition is met). The maximum computational saving corresponds to $L^0/h^0 = 0.5$, for which the CPU time of the implicit calculations is ≈ 50 times less, and the minimum computational saving corresponds to the longest cell length considered $L^0/h^0 = 6$, for which the implicit calculation is completed in a CPU time which is ≈ 30 times less. Moreover, note that the CPU time for the calculations with the UMAT increases with L^0/h^0 due to the increase of the number of elements with the cell size. In contrast, for the explicit calculations, the computational time decreases, reaches a minimum for an intermediate cell size, and then increases. In this case, the CPU time seems to be a balance between the increase of the number of elements with L^0/h^0, and the decrease

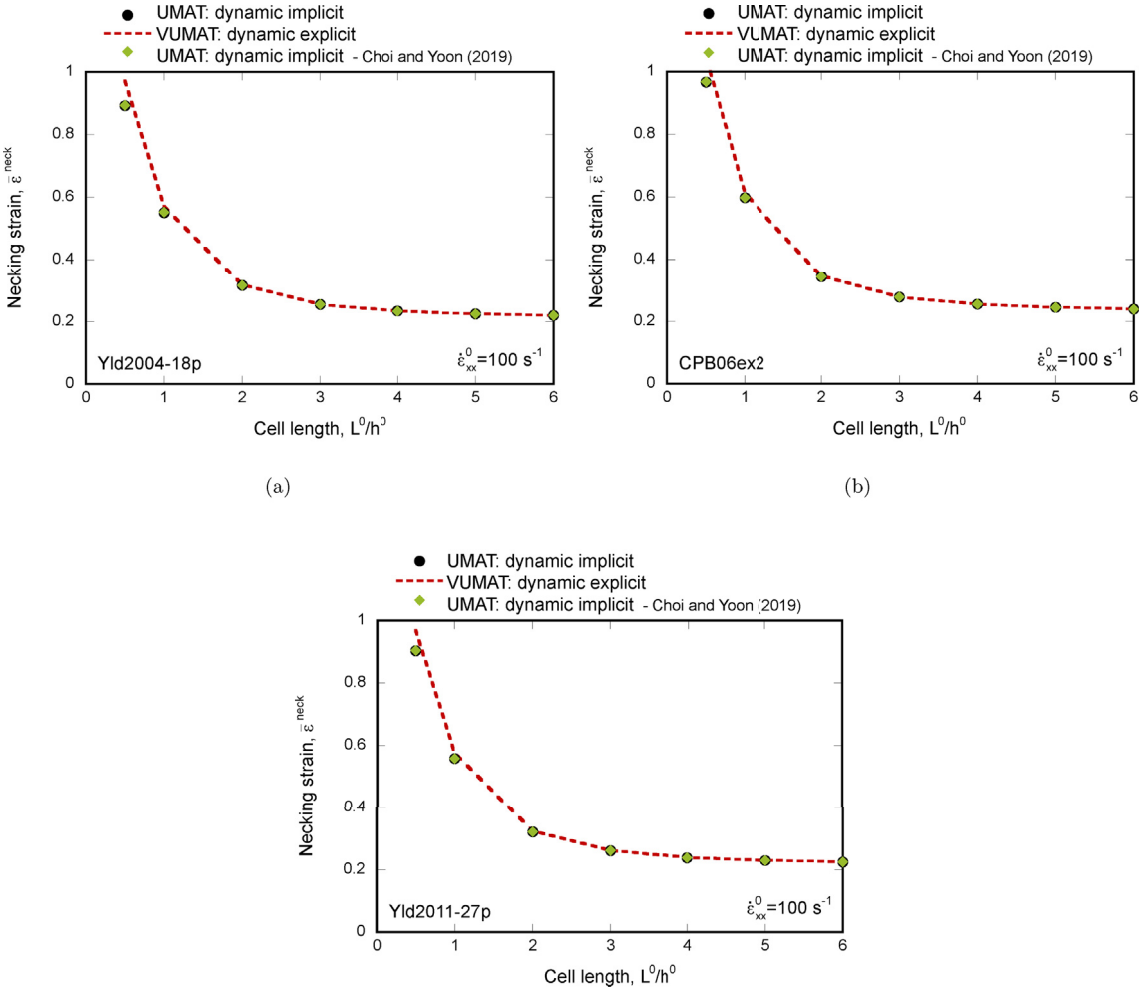

Fig. 8. Finite element results. Evolution of the necking strain $\bar{\varepsilon}^{neck}$ with the cell length L^0/h^0. Comparison between dynamic implicit and explicit simulations performed with UMAT and VUMAT subroutines, respectively. The imposed initial strain rate is $\dot{\varepsilon}^0_{xx} = 100$ s^{-1}. The results are obtained with the numerical approximation of the yield function gradients of Section 5 and the numerical differentiation scheme proposed by Choi and Yoon [1]; which is shown in Appendix B. The calculations are performed with three yield criteria: (a) Yld2004-18p-N, (b) CPB06ex2-N and (c) Yld2011-27p-N.

Table 7
CPU time for plane strain finite element simulations performed with the three yield criteria presented in Section 2. The CPU time is taken approximately when the necking condition is met. The imposed initial strain rate is $\dot{\varepsilon}^0_{xx} = 100$ s^{-1}. Comparison between dynamic implicit and explicit simulations performed with UMAT and VUMAT subroutines, respectively. The results are obtained with the numerical approximation of the yield function gradients of Section 5 and the numerical differentiation scheme proposed by Choi and Yoon [1]; which is shown in Appendix B.

CPU time (units in kiloseconds)

Cell length	Yld2004-18p			CPB06ex2			Yld2011-27p		
	UMAT	UMAT - Choi and Yoon [1]	VUMAT	UMAT	UMAT - Choi and Yoon [1]	VUMAT	UMAT	UMAT - Choi and Yoon [1]	VUMAT
0.5	0.186	0.252	52.877	0.251	0.216	54.118	0.265	0.273	61.560
1	0.260	0.368	23.880	0.288	0.346	24.600	0.321	0.479	28.500
2	0.409	0.525	19.500	0.400	0.522	20.820	0.519	0.728	26.580
3	0.581	0.762	22.440	0.568	0.763	23.760	0.728	0.994	31.020
4	0.753	0.991	26.700	0.757	0.977	28.980	0.918	1.233	36.600
5	0.940	1.254	32.580	0.945	1.213	35.160	1.143	1.529	39.660
6	1.107	1.445	37.980	1.093	1.392	37.800	1.657	1.796	52.260

of the simulation/necking time with the increase of the cell size (due to the decrease of the necking strain). The small computational time of these simulations with UMAT will allow to perform efficient large scale calculations of dynamic formability problems (and other localization related problems), within a range of strain rates < 1000 s^{-1} which is less studied in the literature, partly due to the elevated computational cost of performing explicit analyses for intermediate strain rates (e.g. in our previous works, Zaera et al. [59]; N'souglo et al. [42] and Rodríguez-Martínez et al. [57]; the minimum loading rate studied is 500 s^{-1}, 4000 s^{-1} and 5000 s^{-1}, respectively). This research is left as future work. In addition, notice that for the implicit calculations the computational time obtained with the numerical differentiation scheme

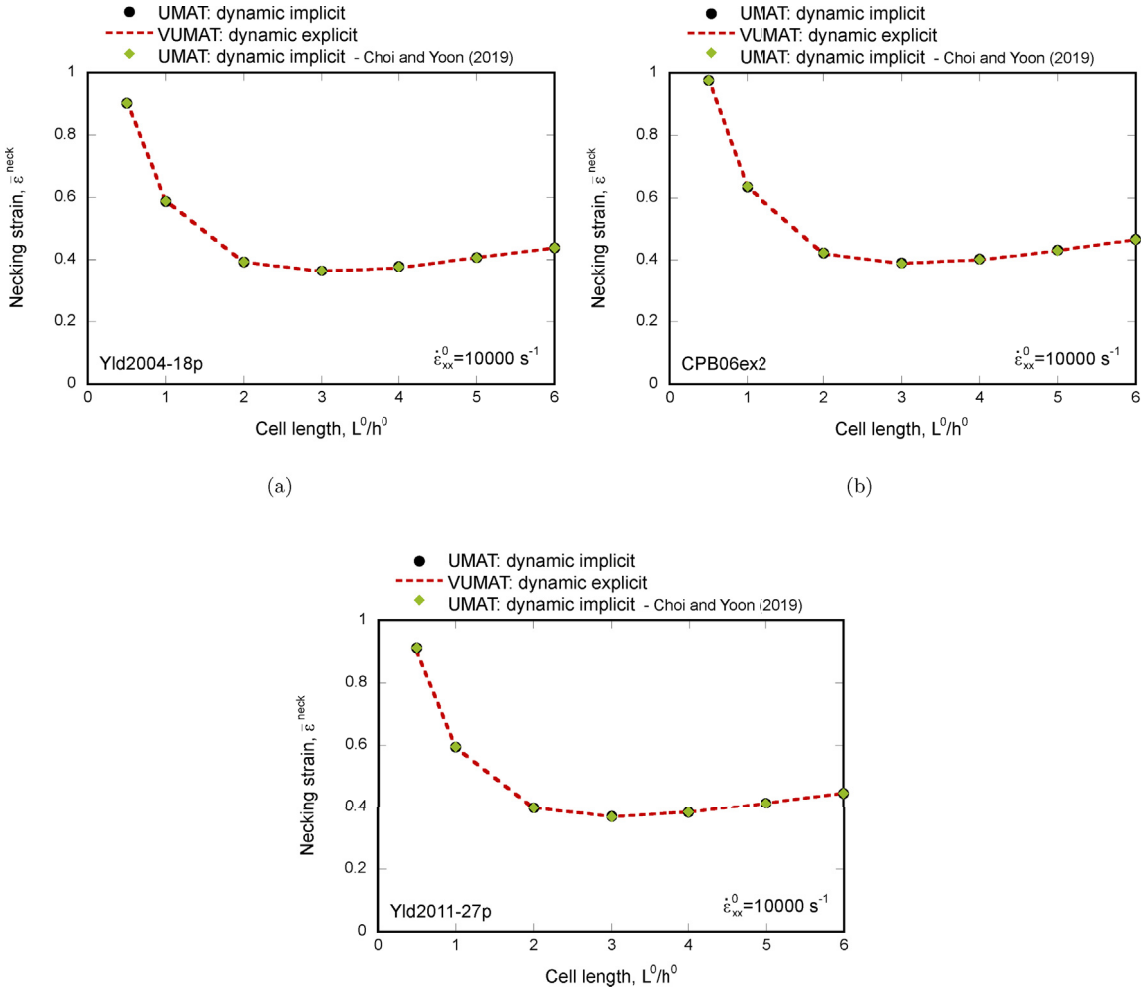

Fig. 9. Finite element results. Evolution of the necking strain $\bar{\varepsilon}^{neck}$ with the cell length L^0/h^0. Comparison between dynamic implicit and explicit simulations performed with UMAT and VUMAT subroutines, respectively. The imposed initial strain rate is $\dot{\varepsilon}^0_{xx} = 10000\ s^{-1}$. The results are obtained with the numerical approximation of the yield function gradients of Section 5 and the numerical differentiation scheme proposed by Choi and Yoon [1]; which is shown in Appendix B. The calculations are performed with three yield criteria: (a) Yld2004-18p-N, (b) CPB06ex2-N and (c) Yld2011-27p-N.

developed in this paper is generally between 5% and 25% lower than in the case of the formulation of Choi and Yoon [1]. This is an original result of this paper which brings out the effect that the specific form of the numerical approximation used for the second derivatives of the yield function gradients has on the computational cost of these simulations.

Fig. 9 shows the evolution of the necking strain $\bar{\varepsilon}^{neck}$ with the cell length L^0/h^0, for greater strain rate $\dot{\varepsilon}^0_{xx} = 10000\ s^{-1}$. Unlike in the case of 100 s^{-1}, the value of $\bar{\varepsilon}^{neck}$ reaches a minimum for an intermediate value of the cell size ≈ 3, and increases for large values of L^0/h^0 due to the influence of inertia, which is more important as the strain rate increases [57,60,61]. The necking strains calculated with the implicit and explicit analyses are very similar, as in the case of the results for the lower strain rate presented in Fig. 8. In contrast, unlike for 100 s^{-1}, the CPU time is greater for the implicit calculations performed with the UMAT, see Table 8. For $L^0/h^0 = 0.5$, using the VUMAT leads to a computational saving which depends on the constitutive model and ranges between 5% and 20% with respect to the implicit calculations performed with the numerical differentiation scheme of Section 5, and for $L^0/h^0 = 6$ the computational saving increases up to 250% for the Yld2011-27p yield criterion. These results bring out that there is a critical loading rate from which implicit analyses are comparatively less efficient than the explicit calculations. The key point is that, in comparison with the simulations performed for 100 s^{-1}, the CPU time decreases two orders of magnitude for the explicit calculations, whereas it increases for the implicit computations, using both the numerical differentiation scheme developed in this paper and the formulation of Choi and Yoon [1]; for most of the cell lengths investigated (it is multiplied by 2 for the greater values of L^0/h^0). Moreover, the computational cost of both implicit and explicit calculations increases with the increase of the cell size. Notice that this was not the case for the explicit calculations for the lower strain rate 100 s^{-1}, for which the CPU time was minimum for an intermediate value of L^0/h^0. The difference is the increase of the necking strain for long wavelengths for 10000 s^{-1}, which is added to the fact that the number of elements increases with L^0/h^0, resulting in a longer CPU time as the cell size increases. Note also that for the implicit calculations, the computational time obtained with the numerical differentiation scheme developed in this paper is between 15% and 40% lower than that obtained with the formulation of Choi and Yoon [1]. This comparative analysis is an original contribution of this paper.

8. Concluding remarks

In this paper we have implemented in ABAQUS three advanced yield criteria using both analytical derivatives and numerical approximations of the yield functions gradients. Specifically, we have developed UMAT and VUMAT subroutines for the Yld2004-18p, CPB06ex2

Table 8
CPU time for plane strain finite element simulations performed with the three yield criteria presented in Section 2. The CPU time is taken approximately when the necking condition is met. The imposed initial strain rate is $\dot{\varepsilon}^0_{xx} = 10000\ s^{-1}$. Comparison between dynamic implicit and explicit simulations performed with UMAT and VUMAT subroutines, respectively. The results are obtained with the numerical approximation of the yield function gradients of Section 5 (denoted with –N) and the numerical differentiation scheme proposed by Choi and Yoon [1]; which is shown in Appendix B.

CPU time (units in kiloseconds)

Cell length	Yld2004-18p-N			CPB06ex2-N			Yld2011-27p-N		
	UMAT	UMAT - Choi and Yoon [1]	VUMAT	UMAT	UMAT - Choi and Yoon [1]	VUMAT	UMAT	UMAT - Choi and Yoon [1]	VUMAT
0.5	0.223	0.444	0.196	0.224	0.266	0.210	0.277	0.344	0.227
1	0.411	0.755	0.228	0.412	0.492	0.237	0.502	0.650	0.259
2	0.752	0.983	0.272	0.755	0.912	0.294	0.916	1.533	0.339
3	1.126	1.336	0.370	1.110	1.353	0.391	1.351	1.853	0.475
4	1.509	1.890	0.551	1.582	1.817	0.560	1.826	2.368	0.653
5	1.934	2.436	0.701	1.977	2.327	0.743	2.304	2.928	0.884
6	2.322	3.556	0.996	2.310	5.379	1.017	2.839	3.576	1.150

and Yld2011-27p models, with material parameters values corresponding to aluminium alloy 2090-T3. We have shown that using the numerical approximation of the yield functions gradients greatly simplifies the implementation of the constitutive models, which is a particularly laborious task for the yield criteria considered in this paper, if the analytical expressions of the stress derivatives are used. Moreover, we have performed cylindrical cup deep drawing test simulations and calculations of dynamic necking localization under plane strain tension using implicit and explicit analyses in ABAQUS/Standard and ABAQUS/Explicit, respectively. The finite element results have shown that, while the explicit analyses performed with the VUMAT are virtually insensitive to the procedure used for the calculation of the yield function gradients, the implicit analyses with the UMAT, which involve the computation of second order yield function gradients, greatly benefit from using the numerical approximation for the stress derivatives, leading to a decrease in the computational time up to 70% for some of the deep drawing calculations performed. In addition, the dynamic necking simulations have brought out that there is a critical value of loading rate below/above which the implicit/explicit analysis is computationally more efficient. For the lower strain rate investigated 100 s^{-1}, the implicit analyses are between 30 and 50 times computationally cheaper than the explicit simulations. In contrast, for the greater strain rate investigated 10000 s^{-1}, the implicit calculations are up to 2.5 times more expensive. Note also that the implicit dynamic necking calculations have been performed with both the numerical differentiation scheme developed in this paper and the formulation proposed by Choi and Yoon [1]; the latter being between 5% and 45% computationally more expensive for the finite element simulations carried out in this work.

Declaration of competing interest

The authors declare that they have no known competing financial interests or personal relationships that could have appeared to influence the work reported in this paper.

Acknowledgements

The research leading to these results has received funding from the European Research Council (ERC) under the European Union's Horizon 2020 research and innovation programme. Project PURPOSE, grant agreement 758056.

The authors express sincere gratitude to Dr. Oana Cazacu (University of Florida) and Dr. Guadalupe Vadillo (University Carlos III of Madrid) for helpful discussions on plastic anisotropy and implementation of the constitutive models in ABAQUS.

Appendix A. Analytical expressions for the stress derivatives

This Appendix shows the analytical expressions for the first and second derivatives of the effective stress with respect to the components of the stress tensor for the three constitutive models presented in Section 2.

Appendix A.1. Yld2004-18p yield criterion

The first derivative of the effective stress with respect to the components of the stress tensor is:

$$\frac{\partial \bar{\sigma}}{\partial \sigma_{ij}} = \frac{\partial \bar{\sigma}}{\partial \phi_{\text{Yld04}}} \frac{\partial \phi_{\text{Yld04}}}{\partial \sigma_{ij}} \tag{A.1}$$

with:

$$\frac{\partial \phi_{\text{Yld04}}}{\partial \sigma_{ij}} = \sum_{a=1}^{3} \sum_{b=1}^{3} \sum_{c=1}^{6} \frac{\partial \phi_{\text{Yld04}}}{\partial \widetilde{S}'_a} \frac{\partial \widetilde{S}'_a}{\partial H'_b} \frac{\partial H'_b}{\partial \widetilde{s}'_c} \frac{\partial \widetilde{s}'_c}{\partial \sigma_{ij}} + \frac{\partial \phi_{\text{Yld04}}}{\partial \widetilde{S}''_a} \frac{\partial \widetilde{S}''_a}{\partial H''_b} \frac{\partial H''_b}{\partial \widetilde{s}''_c} \frac{\partial \widetilde{s}''_c}{\partial \sigma_{ij}} \tag{A.2}$$

where $\widetilde{S}'_a$, H'_b and $\widetilde{s}'_c$ are the principal values, the invariants and the independent components, respectively, of the tensor $\mathbf{s}'$ (see equation (6)). Similarly, $\widetilde{S}''_a$, H''_b and $\widetilde{s}''_c$ denote the same quantities for the tensor $\mathbf{s}''$.

The second derivative is:

$$\frac{\partial^2 \bar{\sigma}}{\partial \sigma_{ij} \partial \sigma_{kl}} = \frac{\partial^2 \bar{\sigma}}{\partial \phi_{\text{Yld04}} \partial \phi_{\text{Yld04}}} \frac{\partial \phi_{\text{Yld04}}}{\partial \sigma_{ij}} \frac{\partial \phi_{\text{Yld04}}}{\partial \sigma_{kl}} + \frac{\partial \bar{\sigma}}{\partial \phi_{\text{Yld04}}} \frac{\partial^2 \phi_{\text{Yld04}}}{\partial \sigma_{ij} \partial \sigma_{kl}} \tag{A.3}$$

with:

$$\begin{aligned}
\frac{\partial^2 \phi_{\text{Yld04}}}{\partial \sigma_{ij} \partial \sigma_{kl}} = & \sum_{a=1}^{3} \sum_{b=1}^{3} \sum_{c=1}^{3} \sum_{d=1}^{3} \sum_{e=1}^{6} \sum_{f=1}^{6} \frac{\partial^2 \phi_{\text{Yld04}}}{\partial \widetilde{S}'_a \partial \widetilde{S}'_b} \\
& \left(\frac{\partial \widetilde{S}'_a}{\partial H'_c} \frac{\partial H'_c}{\partial \widetilde{s}'_e} \frac{\partial \widetilde{s}'_e}{\partial \sigma_{ij}} \right) \left(\frac{\partial \widetilde{S}'_b}{\partial H'_d} \frac{\partial H'_d}{\partial \widetilde{s}'_f} \frac{\partial \widetilde{s}'_f}{\partial \sigma_{kl}} \right) \\
& + \frac{\partial^2 \phi_{\text{Yld04}}}{\partial \widetilde{S}''_a \partial \widetilde{S}''_b} \left(\frac{\partial \widetilde{S}''_a}{\partial H''_c} \frac{\partial H''_c}{\partial \widetilde{s}''_e} \frac{\partial \widetilde{s}''_e}{\partial \sigma_{ij}} \right) \left(\frac{\partial \widetilde{S}''_b}{\partial H''_d} \frac{\partial H''_d}{\partial \widetilde{s}''_f} \frac{\partial \widetilde{s}''_f}{\partial \sigma_{kl}} \right) \\
& + \frac{\partial^2 \phi_{\text{Yld04}}}{\partial \widetilde{S}'_a \partial \widetilde{S}''_b} \left(\frac{\partial \widetilde{S}'_a}{\partial H'_c} \frac{\partial H'_c}{\partial \widetilde{s}'_e} \frac{\partial \widetilde{s}'_e}{\partial \sigma_{ij}} \right) \left(\frac{\partial \widetilde{S}''_b}{\partial H''_d} \frac{\partial H''_d}{\partial \widetilde{s}''_f} \frac{\partial \widetilde{s}''_f}{\partial \sigma_{kl}} \right) \\
& + \frac{\partial^2 \phi_{\text{Yld04}}}{\partial \widetilde{S}''_a \partial \widetilde{S}'_b} \left(\frac{\partial \widetilde{S}''_a}{\partial H''_c} \frac{\partial H''_c}{\partial \widetilde{s}''_e} \frac{\partial \widetilde{s}''_e}{\partial \sigma_{ij}} \right) \left(\frac{\partial \widetilde{S}'_b}{\partial H'_d} \frac{\partial H'_d}{\partial \widetilde{s}'_f} \frac{\partial \widetilde{s}'_f}{\partial \sigma_{kl}} \right) \\
& + \sum_{a=1}^{3} \sum_{b=1}^{3} \sum_{c=1}^{3} \sum_{d=1}^{6} \sum_{e=1}^{6} \frac{\partial \phi_{\text{Yld04}}}{\partial \widetilde{S}'_a} \frac{\partial^2 \widetilde{S}'_a}{\partial H'_b \partial H'_c} \\
& \left(\frac{\partial H'_b}{\partial \widetilde{s}'_d} \frac{\partial \widetilde{s}'_d}{\partial \sigma_{ij}} \right) \left(\frac{\partial H'_c}{\partial \widetilde{s}'_e} \frac{\partial \widetilde{s}'_e}{\partial \sigma_{kl}} \right) \\
& + \frac{\partial \phi_{\text{Yld04}}}{\partial \widetilde{S}''_a} \frac{\partial^2 \widetilde{S}''_a}{\partial H''_b \partial H''_c} \left(\frac{\partial H''_b}{\partial \widetilde{s}''_d} \frac{\partial \widetilde{s}''_d}{\partial \sigma_{ij}} \right) \left(\frac{\partial H''_c}{\partial \widetilde{s}''_e} \frac{\partial \widetilde{s}''_e}{\partial \sigma_{kl}} \right) \\
& + \sum_{a=1}^{3} \sum_{b=1}^{3} \sum_{c=1}^{6} \sum_{d=1}^{6} \frac{\partial \phi_{\text{Yld04}}}{\partial \widetilde{S}'_a} \frac{\partial \widetilde{S}'_a}{\partial H'_b} \frac{\partial^2 H'_b}{\partial \widetilde{s}'_c \partial \widetilde{s}'_d} \left(\frac{\partial \widetilde{s}'_c}{\partial \sigma_{ij}} \right) \left(\frac{\partial \widetilde{s}'_d}{\partial \sigma_{kl}} \right) \\
& + \frac{\partial \phi_{\text{Yld04}}}{\partial \widetilde{S}''_a} \frac{\partial \widetilde{S}''_a}{\partial H''_b} \frac{\partial^2 H''_b}{\partial \widetilde{s}''_c \partial \widetilde{s}''_d} \left(\frac{\partial \widetilde{s}''_c}{\partial \sigma_{ij}} \right) \left(\frac{\partial \widetilde{s}''_d}{\partial \sigma_{kl}} \right) \\
& + \sum_{a=1}^{3} \sum_{b=1}^{3} \sum_{c=1}^{6} \frac{\partial \phi_{\text{Yld04}}}{\partial \widetilde{S}'_a} \frac{\partial \widetilde{S}'_a}{\partial H'_b} \frac{\partial H'_b}{\partial \widetilde{s}'_c} \frac{\partial^2 \widetilde{s}'_c}{\partial \sigma_{ij} \partial \sigma_{kl}} \\
& + \frac{\partial \phi_{\text{Yld04}}}{\partial \widetilde{S}''_a} \frac{\partial \widetilde{S}''_a}{\partial H''_b} \frac{\partial H''_b}{\partial \widetilde{s}''_c} \frac{\partial^2 \widetilde{s}''_c}{\partial \sigma_{ij} \partial \sigma_{kl}}
\end{aligned} \tag{A.4}$$

Appendix A.2. CPB06ex2 yield criterion

The first derivative of the effective stress with respect to the components of the stress tensor is:

$$\frac{\partial \bar{\sigma}}{\partial \sigma_{ij}} = \frac{\partial \bar{\sigma}}{\partial \phi_{\text{CPB06}}} \frac{\partial \phi_{\text{CPB06}}}{\partial \sigma_{ij}} \tag{A.5}$$

where:

$$\frac{\partial \phi_{\text{CPB06}}}{\partial \sigma_{ij}} = \sum_{a=1}^{3}\sum_{b=1}^{3}\sum_{c=1}^{6} \frac{\partial \phi_{\text{CPB06}}}{\partial \widetilde{S}'_a} \frac{\partial \widetilde{S}'_a}{\partial H'_b} \frac{\partial H'_b}{\partial \widetilde{s}'_c} \frac{\partial \widetilde{s}'_c}{\partial \sigma_{ij}} + \frac{\partial \phi_{\text{CPB06}}}{\partial \widetilde{S}''_a} \frac{\partial \widetilde{S}''_a}{\partial H''_b} \frac{\partial H''_b}{\partial \widetilde{s}''_c} \frac{\partial \widetilde{s}''_c}{\partial \sigma_{ij}} \tag{A.6}$$

and the second derivative is:

$$\frac{\partial^2 \bar{\sigma}}{\partial \sigma_{ij} \partial \sigma_{kl}} = \frac{\partial^2 \bar{\sigma}}{\partial \phi_{\text{CPB06}} \partial \phi_{\text{CPB06}}} \frac{\partial \phi_{\text{CPB06}}}{\partial \sigma_{ij}} \frac{\partial \phi_{\text{CPB06}}}{\partial \sigma_{kl}} + \frac{\partial \bar{\sigma}}{\partial \phi_{\text{CPB06}}} \frac{\partial^2 \phi_{\text{CPB06}}}{\partial \sigma_{ij} \partial \sigma_{kl}} \tag{A.7}$$

with:

$$\begin{aligned}
\frac{\partial^2 \phi_{\text{CPB06}}}{\partial \sigma_{ij} \partial \sigma_{kl}} = & \sum_{a=1}^{3}\sum_{b=1}^{3}\sum_{c=1}^{3}\sum_{d=1}^{3}\sum_{e=1}^{6}\sum_{f=1}^{6} \frac{\partial^2 \phi_{\text{CPB06}}}{\partial \widetilde{S}'_a \partial \widetilde{S}'_b} \\
& \left(\frac{\partial \widetilde{S}'_a}{\partial H'_c} \frac{\partial H'_c}{\partial \widetilde{s}'_e} \frac{\partial \widetilde{s}'_e}{\partial \sigma_{ij}}\right)\left(\frac{\partial \widetilde{S}'_b}{\partial H'_d} \frac{\partial H'_d}{\partial \widetilde{s}'_f} \frac{\partial \widetilde{s}'_f}{\partial \sigma_{kl}}\right) \\
& + \frac{\partial^2 \phi_{\text{CPB06}}}{\partial \widetilde{S}''_a \partial \widetilde{S}''_b} \left(\frac{\partial \widetilde{S}''_a}{\partial H''_c} \frac{\partial H''_c}{\partial \widetilde{s}''_e} \frac{\partial \widetilde{s}''_e}{\partial \sigma_{ij}}\right)\left(\frac{\partial \widetilde{S}''_b}{\partial H''_d} \frac{\partial H''_d}{\partial \widetilde{s}''_f} \frac{\partial \widetilde{s}''_f}{\partial \sigma_{kl}}\right) \\
& + \sum_{a=1}^{3}\sum_{b=1}^{3}\sum_{c=1}^{3}\sum_{d=1}^{6}\sum_{e=1}^{6} \frac{\partial \phi_{\text{CPB06}}}{\partial \widetilde{S}'_a} \frac{\partial^2 \widetilde{S}'_a}{\partial H'_b \partial H'_c} \\
& \left(\frac{\partial H'_b}{\partial \widetilde{s}'_d} \frac{\partial \widetilde{s}'_d}{\partial \sigma_{ij}}\right)\left(\frac{\partial H'_c}{\partial \widetilde{s}'_e} \frac{\partial \widetilde{s}'_e}{\partial \sigma_{kl}}\right) \\
& + \frac{\partial \phi_{\text{CPB06}}}{\partial \widetilde{S}''_a} \frac{\partial^2 \widetilde{S}''_a}{\partial H''_b \partial H''_c} \left(\frac{\partial H''_b}{\partial \widetilde{s}''_d} \frac{\partial \widetilde{s}''_d}{\partial \sigma_{ij}}\right)\left(\frac{\partial H''_c}{\partial \widetilde{s}''_e} \frac{\partial \widetilde{s}''_e}{\partial \sigma_{kl}}\right) \\
& + \sum_{a=1}^{3}\sum_{b=1}^{3}\sum_{c=1}^{6}\sum_{d=1}^{6} \frac{\partial \phi_{\text{CPB06}}}{\partial \widetilde{S}'_a} \frac{\partial \widetilde{S}'_a}{\partial H'_b} \frac{\partial^2 H'_b}{\partial \widetilde{s}'_c \partial \widetilde{s}'_d} \left(\frac{\partial \widetilde{s}'_c}{\partial \sigma_{ij}}\right)\left(\frac{\partial \widetilde{s}'_d}{\partial \sigma_{kl}}\right) \\
& + \frac{\partial \phi_{\text{CPB06}}}{\partial \widetilde{S}''_a} \frac{\partial \widetilde{S}''_a}{\partial H''_b} \frac{\partial^2 H''_b}{\partial \widetilde{s}''_c \partial \widetilde{s}''_d} \left(\frac{\partial \widetilde{s}''_c}{\partial \sigma_{ij}}\right)\left(\frac{\partial \widetilde{s}''_d}{\partial \sigma_{kl}}\right) \\
& + \sum_{a=1}^{3}\sum_{b=1}^{3}\sum_{c=1}^{6} \frac{\partial \phi_{\text{CPB06}}}{\partial \widetilde{S}'_a} \frac{\partial \widetilde{S}'_a}{\partial H'_b} \frac{\partial H'_b}{\partial \widetilde{s}'_c} \frac{\partial^2 \widetilde{s}'_c}{\partial \sigma_{ij} \partial \sigma_{kl}} \\
& + \frac{\partial \phi_{\text{CPB06}}}{\partial \widetilde{S}''_a} \frac{\partial \widetilde{S}''_a}{\partial H''_b} \frac{\partial H''_b}{\partial \widetilde{s}''_c} \frac{\partial^2 \widetilde{s}''_c}{\partial \sigma_{ij} \partial \sigma_{kl}}
\end{aligned} \tag{A.8}$$

Appendix A.3. Yld2011-27p yield criterion

The first derivative of the effective stress is:

$$\frac{\partial \bar{\sigma}}{\partial \sigma_{ij}} = \frac{\partial \bar{\sigma}}{\partial \phi_{\text{Yld11}}} \frac{\partial \phi_{\text{Yld11}}}{\partial \sigma_{ij}} \tag{A.9}$$

with:

$$\begin{aligned}
\frac{\partial \phi_{\text{Yld11}}}{\partial \sigma_{ij}} = & \sum_{a=1}^{3}\sum_{b=1}^{3}\sum_{c=1}^{6} \frac{\partial \phi_{\text{Yld11}}}{\partial \widetilde{S}'_a} \frac{\partial \widetilde{S}'_a}{\partial H'_b} \frac{\partial H'_b}{\partial \widetilde{s}'_c} \frac{\partial \widetilde{s}'_c}{\partial \sigma_{ij}} \\
& + \frac{\partial \phi_{\text{Yld11}}}{\partial \widetilde{S}''_a} \frac{\partial \widetilde{S}''_a}{\partial H''_b} \frac{\partial H''_b}{\partial \widetilde{s}''_c} \frac{\partial \widetilde{s}''_c}{\partial \sigma_{ij}} + \frac{\partial \phi_{\text{Yld11}}}{\partial \widetilde{S}'''_a} \frac{\partial \widetilde{S}'''_a}{\partial H'''_b} \frac{\partial H'''_b}{\partial \widetilde{s}'''_c} \frac{\partial \widetilde{s}'''_c}{\partial \sigma_{ij}}
\end{aligned} \tag{A.10}$$

The second derivative reads:

$$\frac{\partial^2\bar{\sigma}}{\partial\sigma_{ij}\partial\sigma_{kl}} = \frac{\partial^2\bar{\sigma}}{\partial\phi_{\mathrm{Yld11}}\partial\phi_{\mathrm{Yld11}}}\frac{\partial\phi_{\mathrm{Yld11}}}{\partial\sigma_{ij}}\frac{\partial\phi_{\mathrm{Yld11}}}{\partial\sigma_{kl}} + \frac{\partial\bar{\sigma}}{\partial\phi_{\mathrm{Yld11}}}\frac{\partial^2\phi_{\mathrm{Yld11}}}{\partial\sigma_{ij}\partial\sigma_{kl}} \tag{A.11}$$

with

$$\begin{aligned}
\frac{\partial^2\phi_{\mathrm{Yld11}}}{\partial\sigma_{ij}\partial\sigma_{kl}} = {} & \sum_{a=1}^{3}\sum_{b=1}^{3}\sum_{c=1}^{3}\sum_{d=1}^{3}\sum_{e=1}^{6}\sum_{f=1}^{6}\frac{\partial^2\phi_{\mathrm{Yld11}}}{\partial\widetilde{S}'_a\partial\widetilde{S}'_b} \\
& \left(\frac{\partial\widetilde{S}'_a}{\partial H'_c}\frac{\partial H'_c}{\partial\widetilde{s}'_e}\frac{\partial\widetilde{s}'_e}{\partial\sigma_{ij}}\right)\left(\frac{\partial\widetilde{S}'_b}{\partial H'_d}\frac{\partial H'_d}{\partial\widetilde{s}'_f}\frac{\partial\widetilde{s}'_f}{\partial\sigma_{kl}}\right) \\
& + \frac{\partial^2\phi_{\mathrm{Yld11}}}{\partial\widetilde{S}''_a\partial\widetilde{S}''_b}\left(\frac{\partial\widetilde{S}''_a}{\partial H''_c}\frac{\partial H''_c}{\partial\widetilde{s}''_e}\frac{\partial\widetilde{s}''_e}{\partial\sigma_{ij}}\right)\left(\frac{\partial\widetilde{S}''_b}{\partial H''_d}\frac{\partial H''_d}{\partial\widetilde{s}''_f}\frac{\partial\widetilde{s}''_f}{\partial\sigma_{kl}}\right) \\
& + \frac{\partial^2\phi_{\mathrm{Yld11}}}{\partial\widetilde{S}'''_a\partial\widetilde{S}'''_b}\left(\frac{\partial\widetilde{S}'''_a}{\partial H'''_c}\frac{\partial H'''_c}{\partial\widetilde{s}'''_e}\frac{\partial\widetilde{s}'''_e}{\partial\sigma_{ij}}\right)\left(\frac{\partial\widetilde{S}'''_b}{\partial H'''_d}\frac{\partial H'''_d}{\partial\widetilde{s}'''_f}\frac{\partial\widetilde{s}'''_f}{\partial\sigma_{kl}}\right) \\
& + \frac{\partial^2\phi_{\mathrm{Yld11}}}{\partial\widetilde{S}'_a\partial\widetilde{S}''_b}\left(\frac{\partial\widetilde{S}'_a}{\partial H'_c}\frac{\partial H'_c}{\partial\widetilde{s}'_e}\frac{\partial\widetilde{s}'_e}{\partial\sigma_{ij}}\right)\left(\frac{\partial\widetilde{S}''_b}{\partial H''_d}\frac{\partial H''_d}{\partial\widetilde{s}''_f}\frac{\partial\widetilde{s}''_f}{\partial\sigma_{kl}}\right) \\
& + \frac{\partial^2\phi_{\mathrm{Yld11}}}{\partial\widetilde{S}''_a\partial\widetilde{S}'_b}\left(\frac{\partial\widetilde{S}''_a}{\partial H''_c}\frac{\partial H''_c}{\partial\widetilde{s}''_e}\frac{\partial\widetilde{s}''_e}{\partial\sigma_{ij}}\right)\left(\frac{\partial\widetilde{S}'_b}{\partial H'_d}\frac{\partial H'_d}{\partial\widetilde{s}'_f}\frac{\partial\widetilde{s}'_f}{\partial\sigma_{kl}}\right) \\
& + \sum_{a=1}^{3}\sum_{b=1}^{3}\sum_{c=1}^{3}\sum_{d=1}^{6}\sum_{e=1}^{6}\frac{\partial\phi_{\mathrm{Yld11}}}{\partial\widetilde{S}'_a}\frac{\partial^2\widetilde{S}'_a}{\partial H'_b\partial H'_c} \\
& \left(\frac{\partial H'_b}{\partial\widetilde{s}'_d}\frac{\partial\widetilde{s}'_d}{\partial\sigma_{ij}}\right)\left(\frac{\partial H'_c}{\partial\widetilde{s}'_e}\frac{\partial\widetilde{s}'_e}{\partial\sigma_{kl}}\right) \\
& + \frac{\partial\phi_{\mathrm{Yld11}}}{\partial\widetilde{S}''_a}\frac{\partial^2\widetilde{S}''_a}{\partial H''_b\partial H''_c}\left(\frac{\partial H''_b}{\partial\widetilde{s}''_d}\frac{\partial\widetilde{s}''_d}{\partial\sigma_{ij}}\right)\left(\frac{\partial H''_c}{\partial\widetilde{s}''_e}\frac{\partial\widetilde{s}''_e}{\partial\sigma_{kl}}\right) \\
& + \frac{\partial\phi_{\mathrm{Yld11}}}{\partial\widetilde{S}'''_a}\frac{\partial^2\widetilde{S}'''_a}{\partial H'''_b\partial H'''_c}\left(\frac{\partial H'''_b}{\partial\widetilde{s}'''_d}\frac{\partial\widetilde{s}'''_d}{\partial\sigma_{ij}}\right)\left(\frac{\partial H'''_c}{\partial\widetilde{s}'''_e}\frac{\partial\widetilde{s}'''_e}{\partial\sigma_{kl}}\right) \\
& + \sum_{a=1}^{3}\sum_{b=1}^{3}\sum_{c=1}^{6}\sum_{d=1}^{6}\frac{\partial\phi_{\mathrm{Yld11}}}{\partial\widetilde{S}'_a}\frac{\partial\widetilde{S}'_a}{\partial H'_b}\frac{\partial^2 H'_b}{\partial\widetilde{s}'_c\partial\widetilde{s}'_d}\left(\frac{\partial\widetilde{s}'_c}{\partial\sigma_{ij}}\right)\left(\frac{\partial\widetilde{s}'_d}{\partial\sigma_{kl}}\right) \\
& + \frac{\partial\phi_{\mathrm{Yld11}}}{\partial\widetilde{S}''_a}\frac{\partial\widetilde{S}''_a}{\partial H''_b}\frac{\partial^2 H''_b}{\partial\widetilde{s}''_c\partial\widetilde{s}''_d}\left(\frac{\partial\widetilde{s}''_c}{\partial\sigma_{ij}}\right)\left(\frac{\partial\widetilde{s}''_d}{\partial\sigma_{kl}}\right) \\
& + \frac{\partial\phi_{\mathrm{Yld11}}}{\partial\widetilde{S}'''_a}\frac{\partial\widetilde{S}'''_a}{\partial H'''_b}\frac{\partial^2 H'''_b}{\partial\widetilde{s}'''_c\partial\widetilde{s}'''_d}\left(\frac{\partial\widetilde{s}'''_c}{\partial\sigma_{ij}}\right)\left(\frac{\partial\widetilde{s}'''_d}{\partial\sigma_{kl}}\right) \\
& + \sum_{a=1}^{3}\sum_{b=1}^{3}\sum_{c=1}^{6}\frac{\partial\phi_{\mathrm{Yld11}}}{\partial\widetilde{S}'_a}\frac{\partial\widetilde{S}'_a}{\partial H'_b}\frac{\partial H'_b}{\partial\widetilde{s}'_c}\frac{\partial^2\widetilde{s}'_c}{\partial\sigma_{ij}\partial\sigma_{kl}} \\
& + \frac{\partial\phi_{\mathrm{Yld11}}}{\partial\widetilde{S}''_a}\frac{\partial\widetilde{S}''_a}{\partial H''_b}\frac{\partial H''_b}{\partial\widetilde{s}''_c}\frac{\partial^2\widetilde{s}''_c}{\partial\sigma_{ij}\partial\sigma_{kl}} \\
& + \frac{\partial\phi_{\mathrm{Yld11}}}{\partial\widetilde{S}'''_a}\frac{\partial\widetilde{S}'''_a}{\partial H'''_b}\frac{\partial H'''_b}{\partial\widetilde{s}'''_c}\frac{\partial^2\widetilde{s}'''_c}{\partial\sigma_{ij}\partial\sigma_{kl}}
\end{aligned} \tag{A.12}$$

Appendix A.4. Singular cases

The derivatives $\partial\widetilde{S}'_a/\partial H'_b$, with $a = 1,2,3$ and $b = 1,2,3$, are:

$$\frac{\partial\widetilde{S}'_a}{\partial H'_1} = \frac{(\widetilde{S}'_a)^2}{(\widetilde{S}'_a)^2 - 2H'_1\widetilde{S}'_a - H'_2} \tag{A.13a}$$

$$\frac{\partial\widetilde{S}'_a}{\partial H'_2} = \frac{\widetilde{S}'_a}{(\widetilde{S}'_a)^2 - 2H'_1\widetilde{S}'_a - H'_2} \tag{A.13b}$$

$$\frac{\partial\widetilde{S}'_a}{\partial H'_3} = \frac{2}{3\left((\widetilde{S}'_a)^2 - 2H'_1\widetilde{S}'_a - H'_2\right)} \tag{A.13c}$$

which are not defined when:

$$(\widetilde{S}'_a)^2 - 2H'_1\widetilde{S}'_a - H'_2 = 0 \tag{A.14}$$

which leads to:

$$\widetilde{S}'_a = H'_1 \pm \sqrt{(H'_1)^2 + H'_2} \tag{A.15}$$

The comparison of previous expression with equation (8) shows that if $\theta = 0$ the derivatives $\partial\widetilde{S}'_2/\partial H'_b$ and $\partial\widetilde{S}'_3/\partial H'_b$ are not defined; and if $\theta = \pi$ the derivatives which are not defined are $\partial\widetilde{S}'_1/\partial H'_b$ and $\partial\widetilde{S}'_2/\partial H'_b$ (see Barlat et al. [2]). This problem can be circumvented by direct calculation of the derivatives $\partial\varphi/\partial H'_b$, which requires to express φ as a function of H'_b. Nevertheless, such procedure introduces additional complications to the calculation of the effective stress derivatives shown in Appendix A.1, Appendix A.2 and Appendix A.3. Obviously, the same singular cases are encountered in the derivatives $\partial\widetilde{S}''_a/\partial H''_b$ and $\partial\widetilde{S}'''_a/\partial H'''_b$.

Appendix B. Numerical approximations for the stress derivatives proposed by Choi and Yoon [1]

This Appendix shows the numerical approximation of the first and second derivatives of the effective stress with respect to the components of the stress tensor proposed by Choi and Yoon [1] to implement in ABAQUS/Standard various anisotropic constitutive models with distortional hardening under associated and non-associated flow rules. Note that the difference with respect to the numerical differentiation scheme developed in this paper resides in equation (B.3), which in the case of Choi and Yoon [1]; who took the expression from Aretz [41]; involves the calculation of additional terms, increasing the computational time.

Appendix B.1. First derivative approximation

$$\frac{\partial\bar{\sigma}}{\partial\sigma_{ij}} \approx \frac{\bar{\sigma}(\sigma_{ij} + \Delta\sigma_{ij}) - \bar{\sigma}(\sigma_{ij} - \Delta\sigma_{ij})}{2\Delta\sigma_{ij}} \tag{B.1}$$

Appendix B.2. Second derivatives approximation

$$\frac{\partial^2\bar{\sigma}}{\partial\sigma_{ij}\partial\sigma_{ij}} \approx \frac{\bar{\sigma}(\sigma_{ij} - \Delta\sigma_{ij}) - 2\bar{\sigma} + \bar{\sigma}(\sigma_{ij} + \Delta\sigma_{ij})}{\Delta\sigma_{ij}^2} \tag{B.2}$$

$$\frac{\partial^2\bar{\sigma}}{\partial\sigma_{ij}\partial\sigma_{kl}} \approx \frac{\bar{\sigma}(\sigma_{ij} - \Delta\sigma_{ij}, \sigma_{kl} - \Delta\sigma_{kl}) - \bar{\sigma}(\sigma_{ij} - \Delta\sigma_{ij}, \sigma_{kl} + \Delta\sigma_{kl}) - \bar{\sigma}(\sigma_{ij} + \Delta\sigma_{ij}, \sigma_{kl} - \Delta\sigma_{kl}) + \bar{\sigma}(\sigma_{ij} + \Delta\sigma_{ij}, \sigma_{kl} + \Delta\sigma_{kl})}{4\Delta\sigma_{ij}\Delta\sigma_{kl}} \tag{B.3}$$

Appendix C. Supplementary data

Supplementary data to this article can be found online at https://doi.org/10.1016/j.finel.2021.103538.

Credit authors contributions

N. Hosseini: Conceptualization, Formal analysis, Writing, Investigation, Methodology, Software, Validation. J.A. Rodríguez-Martínez: Conceptualization, Formal analysis, Writing, Supervision, Funding acquisition, Project administration.

References

[1] H. Choi, J.W. Yoon, Stress integration-based on finite difference method and its application for anisotropic plasticity and distortional hardening under associated and non-associated flow rules, Comput. Methods Appl. Mech. Eng. 345 (2019) 123–160.
[2] F. Barlat, H. Aretz, J.W. Yoon, M.E. Karabin, J.C. Brem, R.E. Dick, Linear transfomation-based anisotropic yield functions, Int. J. Plast. 21 (5) (2005) 1009–1039.
[3] B. Plunkett, O. Cazacu, F. Barlat, Orthotropic yield criteria for description of the anisotropy in tension and compression of sheet metals, Int. J. Plast. 24 (5) (2008) 847–866.
[4] H. Aretz, F. Barlat, New convex yield functions for orthotropic metal plasticity, Int. J. Non Lin. Mech. 51 (2013) 97–111.
[5] R. Hill, A theory of the yielding and plastic flow of anisotropic metals, in: Proceedings of the Royal Society of London A: Mathematical, Physical and Engineering Sciences, vol. 193, The Royal Society, 1948, pp. 281–297.
[6] R.V. Mises, Mechanik der plastischen formänderung von kristallen, ZAMM - J. Appl. Math. Mech./Z. Angew. Math. Mech. 8 (3) (1928) 161–185.

[7] R. Padmanabhan, M. Oliveira, A. Baptista, J. Alves, L. Menezes, Numerical study on the influence of initial anisotropy on optimal blank shape, Finite Elem. Anal. Des. 45 (2) (2009) 71–80.
[8] S. Koubaa, J. Mars, M. Wali, F. Dammak, Numerical study of anisotropic behavior of aluminum alloy subjected to dynamic perforation, Int. J. Impact Eng. 101 (2017) 105–114.
[9] Y.P. Korkolis, B.R. Mitchell, M.R. Locke, B.L. Kinsey, Plastic flow and anisotropy of a low-carbon steel over a range of strain-rates, Int. J. Impact Eng. 121 (2018) 157–171.
[10] F. Greco, E. Deckers, J. Stroobants, S. Van Poppel, K. Linck, W. Desmet, Finite element simulation of the dynamic behaviour of deep drawn components with accurate thickness description, Finite Elem. Anal. Des. 138 (2018) 12–20.
[11] M. Baral, T. Hama, E. Knudsen, Y.P. Korkolis, Plastic deformation of commercially-pure titanium: experiments and modeling, Int. J. Plast. 105 (2018) 164–194.
[12] O. Cazacu, J.A. Rodríguez-Martínez, Effects of plastic anisotropy on localization in orthotropic materials: new explicit expressions for the orientation of localization bands in flat specimens subjected to uniaxial tension, J. Mech. Phys. Solid. 126 (2019) 272–284.
[13] W. Hu, A novel quadratic yield model to describe the feature of multi-yield-surface of rolled sheet metals, Int. J. Plast. 23 (12) (2007) 2004–2028.
[14] D. Banabic, Sheet Metal Forming Processes: Constitutive Modelling and Numerical Simulation, first ed., Springer Science & Business Media, 2010.
[15] R. Hill, Theoretical plasticity of textured aggregates, Math. Proc. Camb. Phil. Soc. 85 (1) (1979) 179–191.
[16] R. Hill, Constitutive modelling of orthotropic plasticity in sheet metals, J. Mech. Phys. Solid. 38 (3) (1990) 405–417.
[17] W. Tong, Generalized fourth-order Hill's 1979 yield function for modeling sheet metals in plane stress, Acta Mech. 227 (2016) 2719–2733.
[18] F. Barlat, K. Lian, Plastic behavior and stretchability of sheet metals. Part I: a yield function for orthotropic sheets under plane stress conditions, Int. J. Plast. 5 (1) (1989) 51–66.
[19] F. Barlat, O. Richmond, Prediction of tricomponent plane stress yield surfaces and associated flow and failure behavior of strongly textured f.c.c. polycrystalline sheets, Mater. Sci. Eng. 95 (1987) 15–29.
[20] J.F.W. Bishop, R. Hill, A theory of the plastic distortion of a polycrystalline aggregate under combined stress, Phil. Mag. 42 (1951) 414–427.
[21] F. Barlat, D.J. Lege, J.C. Brem, A six-component yield function for anisotropic materials, Int. J. Plast. 7 (7) (1991) 693–712.
[22] W.F. Hosford, A generalized isotropic yield criterion, J. Appl. Mech. 39 (2) (1972) 607–609.
[23] A.P. Karafillis, M.C. Boyce, A general anisotropic yield criterion using bounds and a transformation weighting tensor, J. Mech. Phys. Solid. 41 (12) (1993) 1859–1886.
[24] F. Barlat, R.C. Becker, Y. Hayashida, Y. Maeda, M. Yanagawa, K. Chung, J.C. Brem, D.J. Lege, K. Matsui, S.J. Murtha, S. Hattori, Yielding description for solution strengthened aluminum alloys, Int. J. Plast. 13 (4) (1997) 385–401.
[25] F. Barlat, J.C. Brem, J.W. Yoon, K. Chung, R.E. Dick, D.J. Lege, F. Pourboghrat, S.H. Choi, E. Chu, Plane stress yield function for aluminum alloy sheets—Part I: theory, Int. J. Plast. 19 (9) (2003) 1297–1319.
[26] F. Bron, J. Besson, A yield function for anisotropic materials. application to aluminum alloys, Int. J. Plast. 20 (4) (2004) 937–963.
[27] O. Cazacu, F. Barlat, A criterion for description of anisotropy and yield differential effects in pressure-insensitive metals, Int. J. Plast. 20 (11) (2004) 2027–2045 daniel C. Drucker Memorial Issue..
[28] O. Cazacu, F. Barlat, Generalization of Drucker's yield criterion to orthotropy, Math. Mech. Solid 6 (6) (2001) 613–630.
[29] O. Cazacu, B. Plunkett, F. Barlat, Orthotropic yield criterion for hexagonal closed packed metals, Int. J. Plast. 22 (7) (2006) 1171–1194.
[30] M.E. Nixon, O. Cazacu, R.A. Lebensohn, Anisotropic response of high-purity α-titanium: experimental characterization and constitutive modeling, Int. J. Plast. 26 (4) (2010) 516–532.
[31] A.S. Khan, S. Yu, H. Liu, Deformation induced anisotropic responses of Ti–6Al–4V alloy Part II: a strain rate and temperature dependent anisotropic yield criterion, Int. J. Plast. 38 (2012) 14–26.
[32] C. Raemy, N. Manopulo, P. Hora, On the modelling of plastic anisotropy, asymmetry and directional hardening of commercially pure titanium: a planar fourier series based approach, Int. J. Plast. 91 (2017) 182–204.
[33] B. Kondori, Y. Madi, J. Besson, A. Benzerga, Evolution of the 3D plastic anisotropy of hcp metals: experiments and modeling, Int. J. Plast. 117 (2019) 71–92 ductility Enhancement: Advances in Experimental and Computational Micromechanics - In Honor of Dr. Raja K. Mishra.
[34] N. Park, T.B. Stoughton, J.W. Yoon, A criterion for general description of anisotropic hardening considering strength differential effect with non-associated flow rule, Int. J. Plast. 121 (2019) 76–100.
[35] M.A. Sanz, K. Nguyen, M. Latorre, M. Rodríguez, F.J. Montáns, Sheet metal forming analysis using a large strain anisotropic multiplicative plasticity formulation, based on elastic correctors, which preserves the structure of the infinitesimal theory, Finite Elem. Anal. Des. 164 (2019) 1–17.
[36] J. Lee, H.J. Bong, S.J. Kim, M.G. Lee, D. Kim, An enhanced distortional-hardening-based constitutive model for hexagonal close-packed metals: application to AZ31B magnesium alloy sheets at elevated temperatures, Int. J. Plast. 126 (2020) 102618.
[37] J.W. Yoon, F. Barlat, R.E. Dick, M.E. Karabin, Prediction of six or eight ears in a drawn cup based on a new anisotropic yield function, Int. J. Plast. 22 (1) (2006) 174–193.
[38] F. Grytten, B. Holmedal, O.S. Hopperstad, T. Børvik, Evaluation of identification methods for Yld2004-18p, Int. J. Plast. 24 (12) (2008) 2248–2277.
[39] J.-W. Yoon, F. Barlat, R.E. Dick, K. Chung, T.J. Kang, Plane stress yield function for aluminum alloy sheets—Part II: FE formulation and its implementation, Int. J. Plast. 20 (3) (2004) 495–522 owen Richmond Memorial Special Issue.
[40] G. Vadillo, J. Reboul, J. Fernández-Sáez, A modified gurson model to account for the influence of the lode parameter at high triaxialities, Eur. J. Mech. Solid. 56 (2016) 31–44.
[41] H. Aretz, An advanced numerical differentiation scheme for plastic strain-rate computation, AIP Conf. Proc. 907 (1) (2007) 151–156.
[42] K.E. N'souglo, J.A. Rodríguez-Martínez, O. Cazacu, The effect of tension-compression asymmetry on the formation of dynamic necking instabilities under plane strain stretching, Int. J. Plast. 128 (2020) 102656.
[43] V. Cvitanić, F. Vlak, Ž. Lozina, A finite element formulation based on non-associated plasticity for sheet metal forming, Int. J. Plast. 24 (4) (2008) 646–687.
[44] J.C. Simó, R.L. Taylor, Consistent tangent operators for rate-independent elastoplasticity, Comput. Methods Appl. Mech. Eng. 48 (1) (1985) 101–118.
[45] J.C. Simó, T.J.R. Hughes, Computational Inelasticity, Springer, New York, 1998.
[46] J.W. Yoon, D.Y. Yang, K. Chung, Elasto-plastic finite element method based on incremental deformation theory and continuum based shell elements for planar anisotropic sheet materials, Comput. Methods Appl. Mech. Eng. 174 (1) (1999) 23–56.
[47] D. Banabic, H. Aretz, D.S. Comsa, L. Paraianu, An improved analytical description of orthotropy in metallic sheets, Int. J. Plast. 21 (3) (2005) 493–512.
[48] ABAQUS, Abaqus Explicit v6.6 User's Manual, Version 6, 6 Edition, ABAQUS Inc., Richmond, USA, 2016.
[49] G. Rousselier, F. Barlat, J.W. Yoon, A novel approach for anisotropic hardening modeling. Part I: theory and its application to finite element analysis of deep drawing, Int. J. Plast. 25 (12) (2009) 2383–2409.
[50] I.N. Vladimirov, M.P. Pietryga, S. Reese, Anisotropic finite elastoplasticity with nonlinear kinematic and isotropic hardening and application to sheet metal forming, Int. J. Plast. 26 (5) (2010) 659–687.
[51] A.V. Shutov, C.B. Silbermann, J. Ihlemann, Ductile damage model for metal forming simulations including refined description of void nucleation, Int. J. Plast. 71 (2015) 195–217.
[52] J.-H. Yoon, O. Cazacu, J.W. Yoon, R.E. Dick, Earing predictions for strongly textured aluminum sheets, Int. J. Mech. Sci. 52 (12) (2010) 1563–1578.
[53] Z. Xue, A. Vaziri, J.W. Hutchinson, Material aspects of dynamic neck retardation, J. Mech. Phys. Solid. 56 (2008) 93–113.
[54] A. Needleman, Material rate dependence and mesh sensitivity in localization problems, Comput. Methods Appl. Mech. Eng. 67 (1988) 69–85.
[55] V. Balanethiram, G.S. Daehn, Enhanced formability of interstitial free iron at high strain rates, Scripta Metall. Mater. 27 (12) (1992) 1783–1788.
[56] V. Balanethiram, G.S. Daehn, Hyperplasticity: increased forming limits at high workpiece velocity, Scripta Metall. Mater. 30 (4) (1994) 515–520.
[57] J.A. Rodríguez-Martínez, A. Molinari, R. Zaera, G. Vadillo, J. Fernández-Sáez, The critical neck spacing in ductile plates subjected to dynamic biaxial loading: on the interplay between loading path and inertia effects, Int. J. Solid Struct. 108 (2017) 74–84.
[58] K.E. N'souglo, N. Jacques, J.A. Rodríguez-Martínez, A three-pronged approach to predict the effect of plastic orthotropy on the formability of thin sheets subjected to dynamic biaxial stretching, J. Mech. Phys. Solid. 146 (2021) 104189.
[59] R. Zaera, J.A. Rodríguez-Martínez, G. Vadillo, J. Fernández-Sáez, A. Molinari, Collective behaviour and spacing of necks in ductile plates subjected to dynamic biaxial loading, J. Mech. Phys. Solid. 85 (2015) 245–269.
[60] C. Fressengeas, A. Molinari, Fragmentation of rapidly stretching sheets, Eur. J. Mech. Solid. 13 (1994) 251–268.
[61] S. Mercier, A. Molinari, Predictions of bifurcations and instabilities during dynamic extensions, Int. J. Solid Struct. 40 (2003) 1995–2016.